



## Supplementary Materials for

# The structure of the dynactin complex and its interaction with dynein

Linus Urnavicius, Kai Zhang, Aristides G. Diamant, Carina Motz, Max A. Schlager, Minmin Yu,

Nisha A. Patel, Carol V. Robinson, Andrew P. Carter

correspondence to: [cartera@mrc-lmb.cam.ac.uk](mailto:cartera@mrc-lmb.cam.ac.uk)

### **This PDF file includes:**

Materials and Methods  
Figs. S1 to S19  
Tables S1 to S6  
Captions for Movies S1 to S7  
Full Reference List

### **Other Supplementary Materials for this manuscript includes the following:**

Movies S1 to S7

## Materials and Methods

### Microtubule affinity purification of pig dynactin and dynein

Endogenous dynactin and dynein were purified from pig brains. To obtain high protein yield and purity we used an optimized version of an established protocol (41, 42). Fresh pig brains were obtained from a butcher directly after slaughter and transported in ice-cold phosphate buffered saline (PBS). Two brains (approximately 200 g) were rinsed twice in ice-cold PBS, then the brain stem and main blood vessels were removed manually and the brains were washed again in HB buffer (35 mM PIPES-KOH pH 7.2, 1 mM MgSO<sub>4</sub>, 0.2 mM EGTA, 0.1 mM EDTA, 1 mM DTT). The brains were then mixed with 230 ml HB buffer containing 3 protease inhibitor tablets (Complete-EDTA Free, Roche Applied Science) and 1.3 mM PMSF. Afterwards, the brains were homogenized in a Waring blender using four 15 sec pulses interspersed by 15 sec waits. The lysate was cleared in a TLA16.250 rotor (Beckman Coulter) at 16k rpm for 15 min and subsequently in a Ti70 rotor (Beckman Coulter) at 50k rpm for 30 min (both at 4°C). The supernatant was recovered and microtubules were polymerized by addition of 1 mM Mg-GTP and 20 µM Taxol. After incubation in a water bath at 37°C for 30 min (with gentle mixing every 5 min), the lysate was layered onto an 18 ml 10% (w/v) sucrose cushion (made with HB buffer containing 1mM Mg-GTP and 20 µM Taxol). Microtubules were pelleted through the cushion by centrifugation in a Ti45 rotor (Beckman Coulter) at 45k rpm for 24 min at 25°C. The microtubule pellets were resuspended in a total of 10 ml of release buffer (HB buffer with 10 mM Mg-ATP, 1 mM Mg-GTP, 20 µM Taxol, 100 mM KCl) and re-pelleted in a TLA 100.4 rotor (Beckman Coulter) at 68k rpm for 30 min at 25°C. The supernatant was recovered and loaded onto two 5% to 25% (w/v) linear sucrose gradients (in HB buffer with 0.5 mM Mg-ATP) and spun in a SW28 rotor (Beckman Coulter) at 28k rpm for 17.5 hr at 4°C. The gradient was fractionated into 0.8 ml aliquots. Fractions containing dynein and dynactin were determined by SDS-PAGE (Novex 4-12% Bis-Tris precast gels run in MOPS buffer (Life Technologies)) and western blotting. Dynein was detected using rabbit anti-DHC (polyclonal antibody R-324, Santa Cruz, ac-9115) and mouse anti-DIC (monoclonal antibody, clone 74.1 Merck-Millipore, MAB1618). Dynactin was detected with the p150<sup>Glued</sup> monoclonal antibody, p150Glued (BD Bioscience, 610473). Pooled fractions were loaded onto a MonoQ 5/50 GL column (GE Healthcare) equilibrated in HB buffer. Proteins were eluted with a three phase salt gradient: 0 to 21.5% buffer B (HB buffer with 1 M KCl) in 10 ml, 21.5% to 40% buffer B in 40 ml and 40% to 100% buffer B in 5 ml. The fractions containing dynein or dynactin (identified by SDS-PAGE and western blot) were pooled separately and Mg-ATP was added to a final concentration of 0.1 mM. Dynein and dynactin were both concentrated to a final volume of 50 µl (approximately 3 mg/ml) and separately subjected to size-exclusion chromatography on a TSKgel G4000SW<sub>XL</sub> column with a TSKgel SW<sub>XL</sub> guard column (TOSOH Bioscience) equilibrated in GF150 buffer (25 mM Hepes-KOH pH 7.4, 150 mM KCl, 1 mM MgCl<sub>2</sub>, 0.1 mM Mg-ATP, 5 mM DTT). Dynactin fractions were pooled and concentrated to approximately 1.5 mg/ml (25-30 µl), aliquoted and flash frozen in liquid nitrogen for storage at -80°C. Pooled dynein fractions were supplemented with glycerol to a final concentration of 10% (v/v) before they were concentrated, aliquoted and frozen. A typical yield from 2 brains was approximately 40 µg dynactin and 100 µg of dynein. Protein concentrations were measured using Quick Start Bradford dye (Bio-Rad) and an Ultrospec 2100 Pro spectrophotometer (Amersham).



### Large scale SP-Sepharose purification of pig brain dynactin

Two pig brains were homogenized and cleared as described above. The ultracentrifugation supernatant was filtered through Glass fiber (GF) pre-filters (Sartorius) and 0.45  $\mu$ m syringe filters (Elkay). The filtered lysate was loaded onto an XK 50/30 column (GE Healthcare) packed with 300 ml of SP-Sepharose Fast Flow (GE Healthcare) equilibrated in buffer A (HB buffer with 0.1 mM Mg-ATP). Unbound proteins were washed out with 2 column volumes (CV) of buffer A. Bound proteins were fractionated using a two phase salt gradient: 0% to 25% buffer B (HB buffer with 0.1 mM Mg-ATP and 1 M KCl) in 3 CV and 25% to 100% buffer B in 1 CV. Fractions containing dynactin were determined by SDS-PAGE followed by western blotting for p150<sup>Glued</sup>. The pooled fractions were loaded onto a MonoQ HR 16/10 column (GE Healthcare) equilibrated in 95% HB buffer and 5% buffer C (HB buffer and 1 M KCl). Unbound proteins were washed out with 10 CV 5% buffer C. Dynactin was eluted using a three phase linear gradient: 5% to 15% buffer C in 1 CV, 15% to 35% buffer C in 10 CV and 35% to 100% buffer C in 1 CV. The fractions containing dynactin (identified by SDS-PAGE) were concentrated and subjected to size-exclusion chromatography as described for the microtubule affinity protocol. A typical yield from 2 brains was approximately 1 mg of dynactin. Dynactin from this prep (fig. S1) contains a mixture of p150<sup>Glued</sup> isoforms (p150 and p135) in the ratio approximately 1:5 (p150:p135).

### Cloning, Expression and purification of the human Dynein tail complex

A pACEBac1 Vector containing the Sf9-codon optimized *DYNC1H1* gene with a N-terminal His-ZZ-LTLT tag (13) was used for ligation-independent In-Fusion (Clontech) cloning to generate a C-terminal dynein heavy chain truncation (residues 1-1074). Tail truncations were made with and without a C-terminal *Schistosoma japonicum* Gluthathione-S-Transferase (GST) tag (residues 1-215). The modified pACEBac1 vectors were fused to a pIDC vector that contained the Sf9-optimized genes of human IC2C, LIC2, Tctex1, LC8 and Robl1 by an *in vitro* Cre recombinase (New England Biolabs) mediated reaction (13). The presence of all six genes was verified by PCR. Baculovirus production and insect cell expression of the dynein tail complex was carried out as described previously (13).

For purification, a frozen pellet of 5 liters of Sf9 cell culture was thawed on ice and resuspended in 200 ml lysis buffer (50 mM Hepes-NaOH pH 7.8, 150 mM NaCl, 10% (v/v) glycerol, 0.1 mM Mg-ATP, 5 mM DTT, 2 mM PMSF) supplemented with protease inhibitor (CompleteEDTA Free, Roche Applied Science). Cells were lysed in a 40 ml dounce-type tissue grinder (Wheaton) using 20–30 strokes. After clarification of the lysate by ultracentrifugation (70k rpm, 1 hr, 4°C; Type 70 Ti Rotor, Beckman Coulter), the supernatant was incubated with 10 ml pre-equilibrated IgG Sepharose 6 FastFlow beads (GE Healthcare) in 50 ml Falcon tubes on a roller for 1-2 hr. After incubation, the beads were washed with 100 ml lysis buffer and 200 ml TEV cleavage buffer (50 mM Hepes-KOH pH 7.8, 150 mM KAc, 2 mM MgAc, 1 mM EGTA, 10% (v/v) glycerol, 0.1 mM ATP, 5 mM DTT). The beads were resuspended in 20 ml TEV cleavage buffer containing 200  $\mu$ l TEV protease (4 mg/ml) and incubated in 15 ml Falcon tubes on a roller overnight. After TEV cleavage, the beads were removed and the protein solution concentrated to a volume of 0.5-1 ml using an Amicon Ultracel concentrator (Merck-Millipore) with a 100K molecular weight cut-off. Size-exclusion chromatography was carried out using a Superose6 10/300 column (GE Healthcare) equilibrated in gel filtration buffer (50 mM Hepes-KOH pH 7.8, 150 mM KAc, 2 mM MgAc, 0.1 mM Mg-ATP, 5 mM DTT). Peak

fractions that contained purified dynein tail complex were identified by SDS-PAGE. The fractions of interest were pooled and concentrated to approximately 10 mg/ml (Amicon Ultracel, Merck-Millipore, 100 K molecular weight cut-off concentrator). All purification and concentrating steps were carried out at 4°C. Protein aliquots were flash frozen in liquid nitrogen and stored at -80°C. A typical final yield was 1.7 mg from 5 liter of cells.

#### Size-exclusion chromatography-multi angle light scattering (SEC-MALS)

SEC-MALS employed a Heleos II 18 angle light scattering instrument (Wyatt) coupled to an Optilab refractive index detector (Wyatt). 100 µl of SP-Sepharose prep dynactin at 2.5 mg/ml was run over a TSKgel G4000SW<sub>XL</sub> column with a TSKgel SW<sub>XL</sub> guard column (TOSOH Bioscience) equilibrated in GF150 buffer before passing through the light scattering and refractive index detectors using a standard SEC-MALS format. The observed scattered intensity was used to determine the molar mass from the intercept of the Debye plot (using Zimm's model in the ASTRA software Package (Wyatt)). Measurements were calibrated using bovine serum albumin (Thermo Scientific).

#### BICD2N expression and purification

Residues 1-400 of mouse BICD2 with (BICD2N: GFP-BICD2<sup>1-400</sup>) and without an N-terminal GFP-tag were expressed in Sf9 cells and purified as described in Schlager et. al. 2014 (13).

#### Dynein tail – dynactin – BICD2N (TDB) complex formation

The TDB complex was formed with both the GST-tagged and untagged dynein tail constructs and analyzed by negative stain electron microscopy. The tagged and untagged dynein tails were indistinguishable in 2D class averages of individual particles but the GST-tagged tail showed a more homogenous distribution of particles and was therefore used for the main TDB structure determination.

TDB was prepared for cryo-EM experiments by mixing the GST-tagged dynein tail, SP-Sepharose prep dynactin and BICD2N at a molar ratio of 2:1:14 (0.8 mg of dynactin at approximately 2-4.5 mg/ml) in GF150 buffer. The mixture was incubated on ice for 15-30 min and then run on a TSKgel G4000SW<sub>XL</sub> size-exclusion column with a TSKgel SW<sub>XL</sub> guard column (TOSOH Bioscience) equilibrated in GF150 buffer. The peak containing the TDB triple complex was pooled, concentrated (Amicon Ultracel 100K molecular weight cut-off concentrator: Merck-Millipore) and loaded onto size-exclusion for the second time (fig S13). The peak was concentrated and applied directly to EM grids for freezing as described below.

#### Sypro Ruby staining

Novex 4-12% Bis-Tris precast gels were incubated twice in 100 ml fixation solution (50% (v/v) methanol, 7% (v/v) acetic acid) for 30 min and stained for 14 hr with SYPRO Ruby gel stain solution (Molecular Probes). A 30 min washing step was performed in 100 ml washing solution (10% (v/v) methanol, 7% (v/v) acetic acid). The gels were briefly rinsed with 2 x 100 ml ultrapure water and imaged using a Gel Doc XR+ system with Image Lab 4.0 software (Bio-Rad).

### Cloning and expression of *S.cerevisiae* Dyn1<sup>1-557</sup>

A gene encoding the N-terminal 557 amino acids of the dynein heavy chain (Dyn1<sup>1-557</sup>) of *S.cerevisiae* was commercially synthesized (GeneArt, Invitrogen). This synthetic gene was codon optimized for Sf9 cells, but ultimately expressed in *E. coli*. The gene was cloned into a modified pRSET(A) plasmid, which links a His-lipoyl domain fusion tag to the N-terminus via a TEV cleavage site (43). The resulting plasmid was transformed into SoluBL21 cells (Genlantis), which were grown in 2XTY media supplemented with 7 mg/l ampicillin and 1 mM MgSO<sub>4</sub> at 210 rpm and 37°C. The cultures were grown to an OD<sub>600</sub> between 0.3 and 0.4, cooled to 16°C and induced overnight with 1 mM IPTG. The cells were pelleted by centrifugation at 4k rpm for 20 min (JLA-8.1000 rotor, Beckman Coulter) and then flash frozen in liquid nitrogen and stored at -80°C.

### Purification of *S.cerevisiae* Dyn1<sup>1-557</sup>

Cell pellets from 6 liters of bacterial culture were thawed on ice in 150 ml of bacterial lysis buffer (30 mM Hepes-NaOH pH 7.4, 200 mM NaCl, 2 mM MgCl<sub>2</sub>, 1 mM PMSF, 10 mM imidazole, 10 mM β-mercaptoethanol (BME), 0.1 mM Mg-ATP) supplemented with protease inhibitors (Complete-EDTA Free, Roche Applied Science). This suspension was sonicated on ice at maximum amplitude for 3 min with 3 sec on and 7 sec off pulses. The lysate was cleared by centrifugation in a Ti45 rotor (Beckman Coulter) at 40k rpm for 40 min at 4°C, syringe filtered through a 0.22 μm filter (Elkay) and loaded onto two tandem 5 ml HisTrap columns (GE Healthcare) that were pre-equilibrated in buffer NiA (30 mM Hepes-KOH pH 7.4, 200 mM NaCl, 2 mM MgCl<sub>2</sub>, 10 mM imidazole, 10 mM BME, 0.1 mM Mg-ATP). Unbound proteins were washed off with 50 ml of buffer NiA. The protein of interest was eluted in a single 15 ml fraction with buffer NiB (30 mM Hepes pH 7.4, 200 mM NaCl, 2 mM MgCl<sub>2</sub>, 500 mM imidazole, 10 mM BME, 0.1 mM Mg-ATP). This fraction was exchanged back into buffer NiA by concentrating (30K molecular weight cut-off concentrator, Amicon Ultracel, Merck-Millipore) to approximately 1 ml and diluting with 15 ml of buffer NiA twice. Subsequently, the sample was incubated with 1 ml TEV protease (3.7 mg/ml) and incubated on a roller at 4°C overnight. After TEV cleavage (confirmed by SDS-PAGE), the sample was run back through two tandem 5 ml HisTrap columns (GE Healthcare), pre-equilibrated in buffer NiA. The flowthrough was collected, concentrated to approximately 5 ml and run through a HiLoad 26/600 Superdex200 column (GE Healthcare) that had been pre-equilibrated in GF buffer (30 mM Hepes-NaOH pH 7.4, 200 mM NaCl, 2 mM MgCl<sub>2</sub>, 10 mM BME, 0.1 mM Mg-ATP). This run resulted in two distinct peaks, one near the void volume and the other at the expected elution volume for a dimer of Dyn1<sup>1-557</sup>. The dimer peak was pooled, concentrated to approximately 5 ml and run back through the same column, which was now equilibrated in crystallization buffer (20 mM Tris-NaOH pH 8.0, 150 mM KCl, 10% glycerol (v/v) 1 mM DTT, 0.1 mM Mg-ATP). This run resulted in a single peak of dimerized Dyn1<sup>1-557</sup>, which was pooled, concentrated to approximately 5 mg/ml, aliquoted and flash frozen in liquid nitrogen before storing at -80°C.

### Crystallization of *S.cerevisiae* Dyn1<sup>1-557</sup>

Dyn1<sup>1-557</sup> was crystallized using the hanging drop method in EasyXtal 15-well plates (Qiagen). 1 μl of protein was applied to the screw cap followed by either 0.75 μl or 1 μl of reservoir solution (0.1 M Tris-NaOH pH 8.5, 0.2 M Li<sub>2</sub>SO<sub>4</sub>, 10-12.5% (v/v) PEG8K). Before screwing the cap back on the well, 500 μl of Al's oil (Hampton Research) was applied on top of the 500 μl of reservoir solution already in the well. Crystals grew overnight at 18°C to a

maximum size of 500  $\mu\text{m}$  x 80  $\mu\text{m}$  x 80  $\mu\text{m}$ . Crystals were briefly soaked in a cryo-protectant solution (0.1 M Tris-NaOH pH 8.5, 0.2 M  $\text{Li}_2\text{SO}_4$ , 10-12.5% (v/v) PEG8K, 30% ethylene glycol (v/v)) before being flash frozen in liquid nitrogen.

#### Selenomethionine derivative of Dyn1<sup>1-557</sup>

Since no homology models were available for molecular replacement, we prepared a selenomethionine derivative of Dyn1<sup>1-557</sup> (SeMet) for experimental phasing. The plasmid described above was transformed into B834 (DE3) cells (Novagen), which were grown in M9 media supplemented with 2 mM  $\text{MgSO}_4$ , 0.4% (w/v) glucose, 25 mg/l  $\text{FeSO}_4 \cdot 7\text{H}_2\text{O}$ , 7 mg/l ampicillin, 1 mg/l each of riboflavin, niacinamide, pyridoxine monohydrochloride and thiamine, 40 mg/l each of L-alanine, L-arginine, L-asparagine, L-aspartic acid, L-cysteine, L-glutamic acid, L-glutamine, L-glycine, L-histidine, L-isoleucine, L-leucine, L-lysine, L-phenylalanine, L-proline, L-serine, L-threonine, L-tryptophan, L-tyrosine, L-valine and seleno-L-methionine. Cells were grown at 210 rpm and 30°C until  $\text{OD}_{600} = 0.8-1.0$ . They were induced with 0.3 mM IPTG and grown at 16°C for another 12 hr and harvested as above. SeMet protein was purified in the same way as native protein except to minimize oxidation, all buffers were made with double the amount of BME or DTT and were thoroughly degassed before use. SeMet crystals were obtained and harvested in the same way as native crystals.

#### Data collection, phasing and model building

All data were collected at beamline i03 of Diamond Light Source. The data were integrated using IMOSFLM (44) and scaled using AIMLESS (45). Experimental phase information was obtained employing the MIRAS approach (Multiple isomorphous replacement with anomalous scattering) in autoSHARP (46) with a native data set and three SeMet data sets as derivatives (Table S5). All data sets were cut at 5Å because including higher resolution data did not improve map quality. The resulting 5Å map revealed density for two protein molecules in the asymmetric unit. The map was of sufficient quality to resolve  $\alpha$ -helices, a  $\beta$ -sheet and several loops, which allowed an initial model to be constructed in COOT (47). Model building was aided by an anomalous difference map calculated in CCP4 program FFT (48) using the experimental phases and the amplitudes from SeMet peak data set.

#### Fitting the crystal structure into the EM density

To fit the crystal structure into the EM density map, the full crystal structure was divided into three fragments: the dimerization domain (residues 1 to 179 from chains A and B) and the two elongated domains (chain A and chain B). All three fragments were fitted into the EM density independently using the “jiggle” command in COOT (47). The positions of individual helices in the elongated domains were fitted by minor adjustments.

#### Electron microscopy

Dynactin samples from both affinity and SP-sepharose preps were used for data collection. Samples were diluted to approximately 70-85  $\mu\text{g/ml}$  using buffer containing 150 mM KCl, 5 mM DDT, 0.1 mM Mg-ATP, 1 mM  $\text{MgCl}_2$  and 25 mM  $\text{KH}_2\text{PO}_4$ - $\text{K}_2\text{HPO}_4$  at pH 6.5. TDB samples were diluted to similar concentration in GF150 buffer. In both cases the samples were cross-linked by addition of 0.05% (v/v) glutaraldehyde (Sigma Aldrich) and incubated on ice for 30 to 60 min before making cryo-grids. 3  $\mu\text{l}$  aliquots of the cross-linked samples were applied to plasma treated Quantifoil R1.2/1.3 or R2/2 400-square-mesh copper grids on which a homemade

continuous carbon film had been deposited. Samples were incubated on grids in a Vitrobot III or IV for 15 to 30 sec and blotted for approximately 3-5 sec at 100% humidity and 4°C. Electron micrographs were recorded on a back-thinned Falcon II detector fitted to either a FEI Titan Krios or a FEI Tecnai G2 Polara, both operating at 300kV. Micrographs were collected as movies (recorded at 16 or 17 frames per sec). They were either acquired manually or automatically (EPU, FEI) with a defocus between 2 and 7 $\mu$ m. Four dynactin datasets and one TDB dataset were collected (Table S1). Although particles of dynactin showed high contrast in thin ice, the complex fell apart when the ice was too thin. We therefore used ice that was thick enough to allow most of the particles to stay intact, but thin enough to have reasonable contrast. Each dataset was collected over multiple 24 hr microscope sessions. Pixel size, exposure time and dose are given in Table S1.

Negative stained images of dynactin and TDB were used to obtain initial models, which were then scaled and used as references for the subsequent cryo-EM reconstruction. For dynactin a random conical tilt series (49) was collected at 3.3Å/pix on a FEI Tecnai G2 Spirit transmission electron microscope operating at 120kV and fitted with a Gatan Ultrascan 1,000 XP CCD detector. The dataset for TDB was collected using a single tilt.

#### Image processing

The micrographs for each dataset (Table S1) were corrected for beam-induced drift by aligning the individual frames of each movie using whole-image motion correction (50). Particles were picked automatically using Relion (51) or Gautomatch (by K.Z., under development) and checked manually. CTF parameters for drift corrected micrographs were estimated using CTFFIND3 (52) or a GPU accelerated program Gctf (by K.Z., under development). Subsequently micrographs were rejected if they had a drift larger than 1Å between the first and second frame or 8Å between the first and last frame. Micrographs were also rejected if they had too few good particles (<10), a large astigmatism (>0.3  $\mu$ m), extreme defocus values (<2.0  $\mu$ m or >7.0  $\mu$ m), abnormal Fourier patterns, or too much contamination or aggregation. Automatically picked particles from the remaining good micrographs were then manually screened using the GUI in Relion-1.3. This yielded 446,308 dynactin particles in the low magnification (Dynactin-1) dataset, 697,360 dynactin particles in the combined high magnification (Dynactin-2,3,4) datasets and 257,608 particles in the TDB dataset (Table S1). The best quality particles were selected from these particle sets by multiple cycles of 2D classification. Following this step ~85% of dynactin particles fell into classes with a similar dominant view. To obtain the best 3D reconstruction we needed a balanced distribution of dynactin orientations. We therefore rejected around three quarters of dynactin particles in these dominant view classes.

The 3D reconstructions were performed with starting models calculated from negative stain data and filtered to 60Å. The independent initial models all converged to the same result. Several cycles of 3D classification and refinement were used to further select the particles for final refinement. The selected dynactin particles were corrected for beam induced movement and radiation damage (*B*-factor weighting) before final refinement (53). The final refinement of the TDB and low magnification (Dynactin-1) datasets resulted in 8.2 and 6.3Å maps respectively. The Dynactin-1 dataset was further processed to extract a sub-class of 12,870 particles with obvious extra density (fig. S7). These particles were used to generate an 8.6Å map in which the

p150<sup>Glued</sup>/p135 projection is docked against the side of the dynactin filament. This structure was validated by repeating the reconstruction with a starting model calculated from the particles that did not contain the extra density.

The high magnification datasets (Dynactin-2,3,4) were first processed to obtain independent 3D reconstructions which were used to calculate the scaling factors between them. The raw particles from datasets Dynactin-2 and Dynactin-4 were then scaled using the calculated factors to a final pixel size of 1.34Å. All particles were corrected for beam induced movement and radiation damage before combining them. The best 115,044 particles of the combined dataset were used to yield a final 3D reconstruction with a resolution of 4.0Å overall and 3.5Å for the dynactin filament.

All density maps were corrected for the modulation transfer function (MTF) of the detector, and then sharpened by applying negative B-factors (54).

#### Tilt pair validation

Tilt pairs were used to validate dynactin low magnification and TDB final maps. Electron micrographs were recorded at a 0° and 20° tilt angle (1 and 2 sec exposure time was used respectively) using an ultra-backthinned Falcon III detector fitted to FEI Tecnai G2 Polara operating at 300 kV with a pixel size of 1.7Å (16.5 e<sup>-</sup>/(sec·Å<sup>2</sup>)). The images were recorded at approximately 7µm defocus. Movies were recorded at 16 frames per second and corrected for beam-induced drift by aligning the individual frames of each movie using whole-image motion correction (50). CTF parameters for drift corrected micrographs were estimated using CTFFIND3 (52). Particle pairs were picked manually within EMAN2 (55): TDB 1,680 pairs from 75 micrographs; dynactin 2,883 pairs from 59 micrographs. 2D classification of dynactin particles was used to preferentially discard approximately 70% of particles with the dominant view in order to obtain a balanced orientation as was done for the original refinement. TDB and dynactin particle pairs were combined with the cleaned particles used for the final refinement of the corresponding structure. The 3D refinement was conducted using the combined particles and the final maps low pass filtered to 60Å resolution. After the 3D refinement angular parameters of the particles pairs were extracted and analyzed using Xmipp (56).

#### TDB structure determination using BICD2N, TDB (no GFP)

To confirm the identity of the globular density connected to the BICD2N next to the barbed end of dynactin (Fig. 5B, table S1: TDB1), the structure of a TDB complex containing BICD2<sup>1-400</sup> without a N-terminal GFP-tag was determined (table S1: TDB (no GFP)). Sample preparation and cryo-EM data collection were performed as described above except the sample was run over the size exclusion column only once. 464 micrographs were collected, drift corrected (50) and subjected to CTFFIND3 (52). Automated particle picking was conducted within RELION as for TDB1. 21,204 auto picked particles were first cleaned by 2D classification. The cleaned particle set was used to perform 3D refinement using the TDB1 structure, low pass filtered to 50Å resolution, as an initial reference. The resulting TDB (no GFP) structure was identical to the TDB1 but lacked the previously observed globular domain. Subsequently the particles were subjected to 3D classification. All of the four obtained classes lacked the globular density. The class with the largest particle number and highest alignment accuracy was used for small angle refinement to generate the final map (table S1: TDB (no

GFP)). To compare TDB structures with and without GFP we selected a subset of the original TDB dataset (see table S1: TDB2) in order to produce a map of equivalent resolution to TDB (no GFP).

### Model building and refinement

The atomic models for pig Arp1, Arp11,  $\beta$ -actin were built de novo into density using predicted models from the Phyre2 web server (57) as a guide using COOT (47). The complete filament was refined using Refmac5 (58) and COOT iteratively. Only coordinates were refined while the maps were kept the same after each cycle of refinement (in contrast to crystallographic refinement). Statistics of the refinement are given in Table S3. Models for pig CapZ $\alpha\beta$ , p25 and p27 were predicted using the Phyre2 web server and fitted into the electron density map as a rigid body using Chimera (59). All side chains were cut off after rigid body fitting and the backbones were flexibly refined in real space under tight stereochemical and secondary structural restraints in COOT (47). The helix bundle model of the dynactin shoulder domain and p62 was built by placing poly-alanine chains into the density with strict restraints for helices. The model building and refinement is summarized in table S2.

### Map visualization and analysis

Maps and models were visualized in Chimera (59), COOT (47) and Pymol (<http://www.pymol.org>). Maps of different subunits were segmented within Chimera. Detailed interactions between subunits were analyzed in COOT (47). Figures and movies were made in Pymol and Chimera. Local resolution of the maps was analyzed by ResMap using confidence level (p-value) of 0.05 and 1 Å step size (60).

### Native mass spectrometry

Dynactin from the SP-sepharose prep was buffer exchanged into 150 mM ammonium acetate pH 7.5 using Vivaspin 30K concentrators (Sartorius) prior to mass spectrometry analyses. All spectra were acquired on a QToF II mass spectrometer (Waters, Manchester, UK) modified for analysis of high mass complexes (61). 2.5  $\mu$ l of a 10  $\mu$ M solution was introduced into the mass spectrometer using a gold-coated capillary needle prepared in-house (62). The instrument parameters were as follows: capillary voltage 1.7 kV, cone voltage 100 V, extractor 10 V, collision voltage 35 V, backing pressure  $4.7 \times 10^{-3}$  –  $6.6 \times 10^{-3}$  mbar. For MS/MS experiments, collision voltages varied up to 200 V. All spectra were processed with MassLynx V4.1 (Waters, Manchester, UK) with minimal smoothing and were calibrated externally using 100 mg/ml cesium iodide in water.

### Denaturing protein LC-MS

0.1 mg dynactin complex diluted in water was separated on a Chromolith RP 18 5-2 mm column (Merck Ltd) over a 4 min gradient from 5% to 100% solvent B (solvent B acetonitrile (ACN): solvent A 0.1% formic acid (aq.)). Eluted proteins were analyzed directly on a LCT Premier mass spectrometer (Waters, Manchester, UK). Data were processed with MassLynx V4.1 and spectra were deconvoluted using MaxEnt algorithm.

### Label-free quantitative proteomics

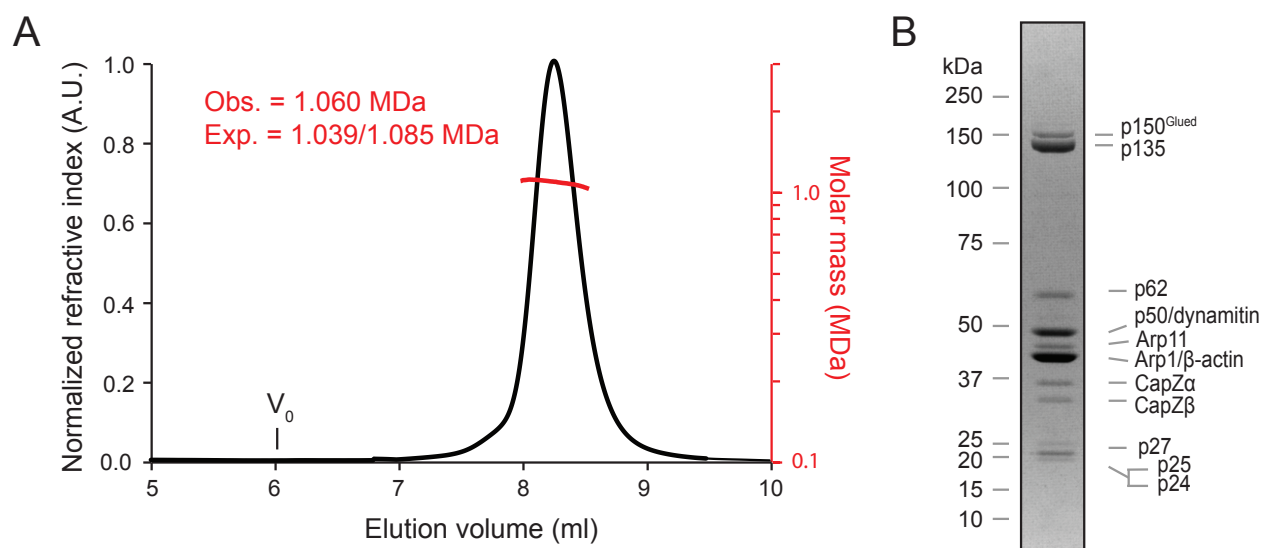
50  $\mu$ g dynactin was digested using 0.3% Rapigest (Waters, Manchester, UK) according to the manufacturer's protocol. The resulting tryptic peptides were reconstituted in 1% formic acid

prior to proteomic analyses. For LC-MS/MS analysis, tryptic peptides were separated by nano-flow reversed-phase liquid chromatography (easy-nLC 1000, Thermo Scientific) (mobile phase A, 0.1% formic acid (aq.); mobile phase B, ACN/0.1% formic acid) coupled to a LTQ-Orbitrap XL hybrid mass spectrometer (Thermo Scientific). The peptides were loaded onto a trap column (HPLC column Acclaim® PepMap 100, 2 cm, C18, 100 µm I.D. particle size 5 µm; Thermo scientific) and separated with a flow rate of 250 nl/min on an analytical C18 capillary column (50 cm, HPLC column Acclaim® PepMap 100, C18, 75 µm I.D. particle size 3 µm; Thermo Scientific), with a gradient of 5-30 % (v/v) mobile phase B over 30 min. Peptides were directly eluted into the mass spectrometer.

Typical mass spectrometry conditions were: spray voltage of 1.6 kV; capillary temperature of 180°C; normalized collision energy of 35% at an activation of  $q = 0.25$  and an activation time of 30 ms. The LTQ-Orbitrap XL was operated in data-dependent mode. Survey full scan mass spectra were acquired in the Orbitrap ( $m/z$  300–2000) with a resolution of 30,000 at  $m/z$  400 and an automatic gain control (AGC) target at  $10^6$ . The five most intense ions were selected for CID MS/MS fragmentation in the linear ion trap at an AGC target of 30,000. Detection in the linear ion trap of previously selected ions was dynamically excluded for 30 sec. Singly charged ions as well as ions with unrecognized charge state were also excluded. Internal calibration of the Orbitrap was performed using the lock mass option (lock mass:  $m/z$  445.120025) (63).

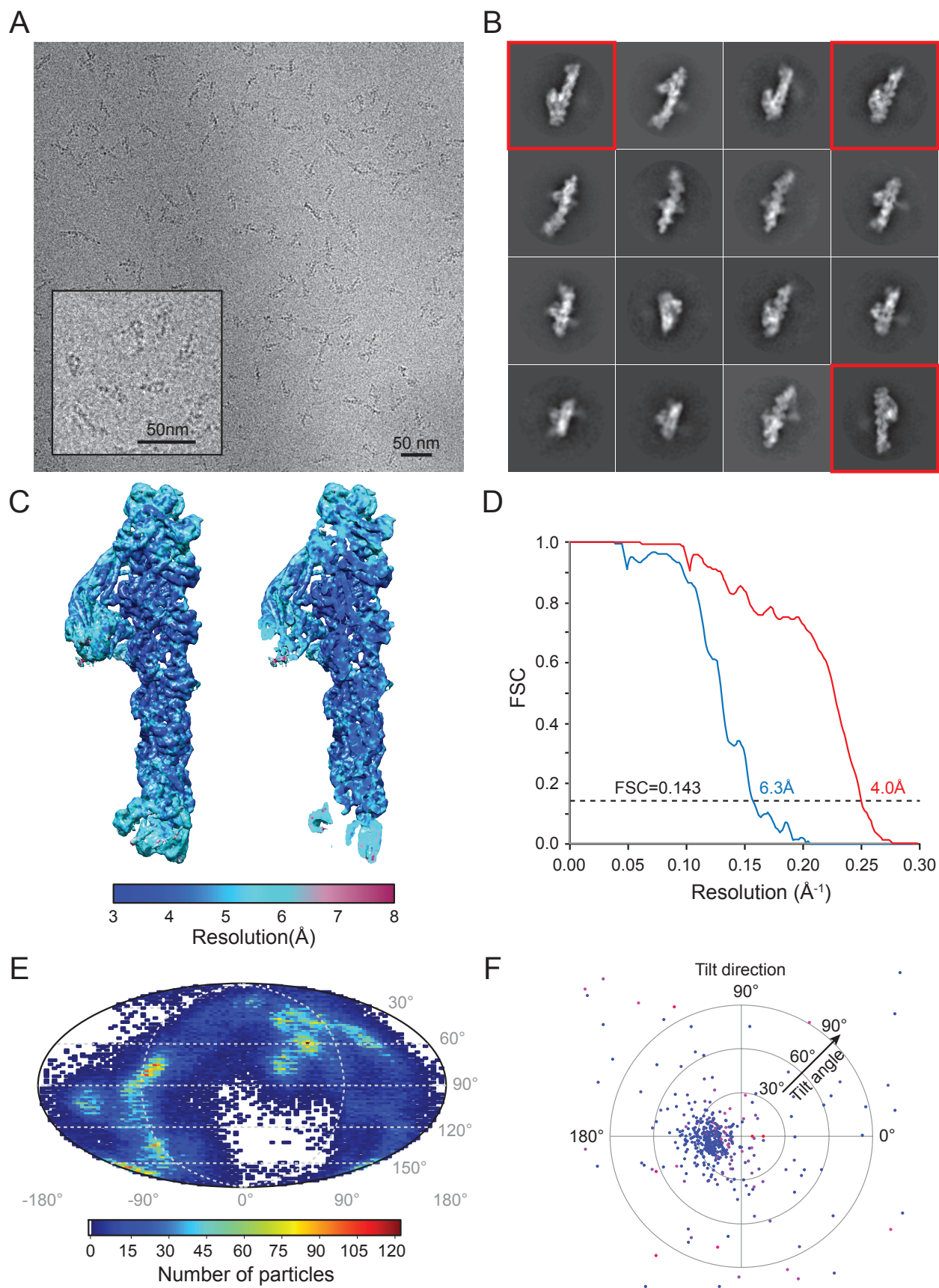
Data were processed against a database containing pig dynactin protein sequences using MaxQuant (64). A fixed modification of carbamidomethyl-C was specified. Variable modifications considered included deamidation N, deamidation Q and oxidation M. Automatic settings for mass accuracy were used and two missed tryptic cleavages were allowed. Relative quantification was achieved by using the label-free quantification method iBAQ. In brief, quantification is achieved by summing all observed peptide intensities and normalizing to the molecular weight of the protein by dividing by the number of theoretically observable peptides (65).





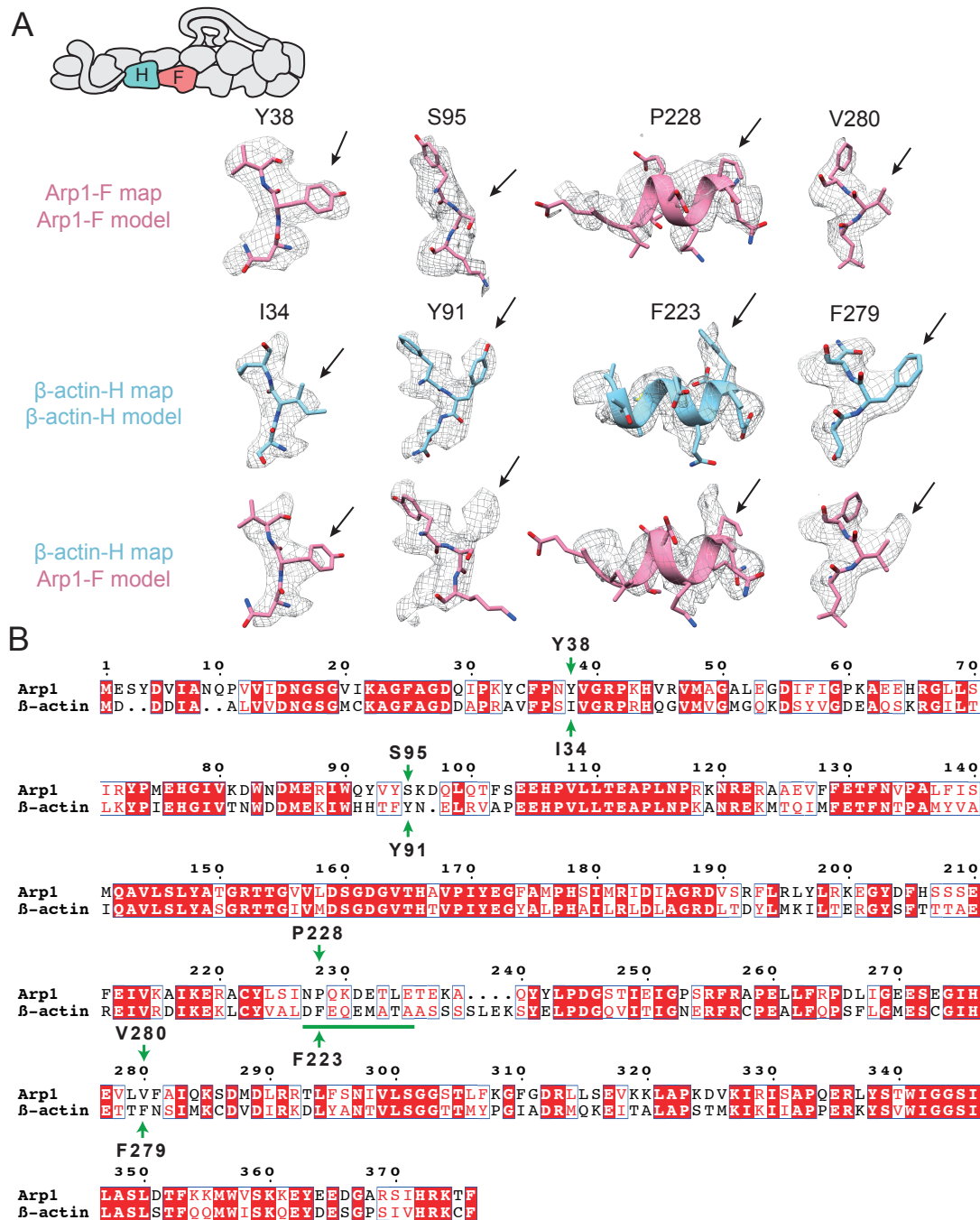
**Fig. S1.**

**Dynactin is a 1.0 MDa complex composed of 12 different proteins.** (A) SEC-MALS of pig dynactin purified from brain tissue. Mean observed molar mass (Obs.) and expected (Exp.) molar masses are indicated.  $V_0$  indicates the void volume of the column. (B) Coomassie stained SDS-PAGE gel of dynactin.



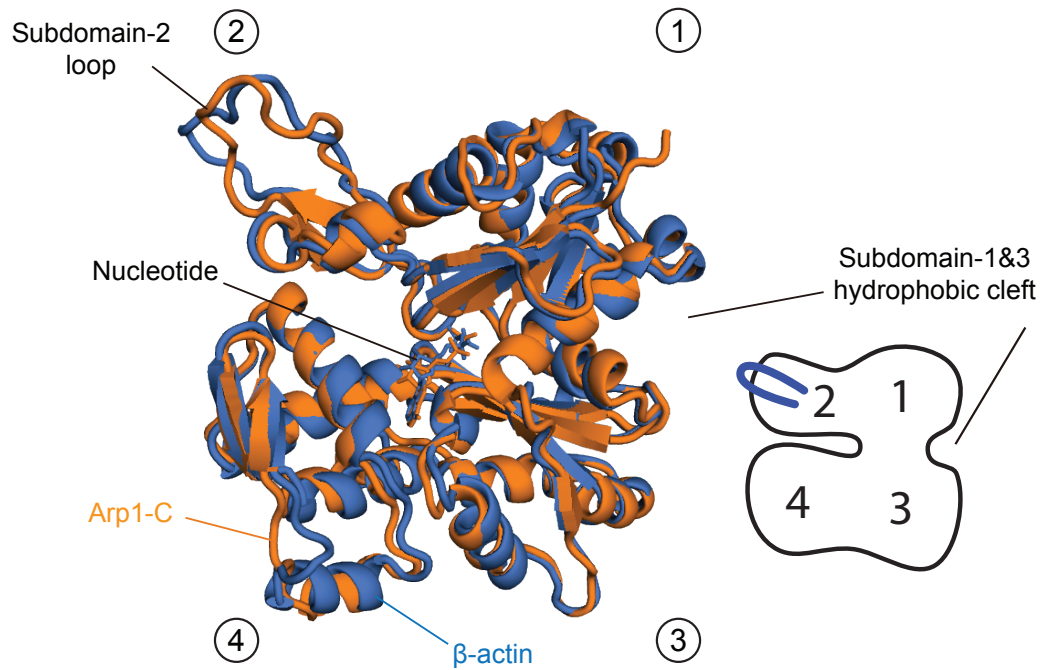
**Fig. S2.**

**Single particle cryo-EM analysis of pig dynactin.** (A) A representative micrograph of dynactin. (B) Typical 2D class averages obtained after preferentially discarding particles with the dominant view (marked with red boxes). (C) The final dynactin map acquired from a higher magnification data set was analyzed by ResMap (60) showing a resolution distribution from 4 to 4.5Å. Interior parts of the map have resolution of ~3.5Å. (D) The gold-standard FSC curves of the final maps (low and high magnification maps in blue and red respectively). The resolutions at FSC=0.143 are 6.3Å and 4.0Å. (E) An equal area projection map of the orientation angles of the final 80,865 particles. (F) Tilt-pair analysis of the 6.3Å dynactin map. Images were recorded at 0° and 20° tilt angle. The position of each dot represents the direction and angle for a particle pair in polar coordinates. In-plate and out-of-plane tilt transformations are shown in blue and red respectively. The blue dots cluster at a tilt angle of approximately 20°, which validates the structure.



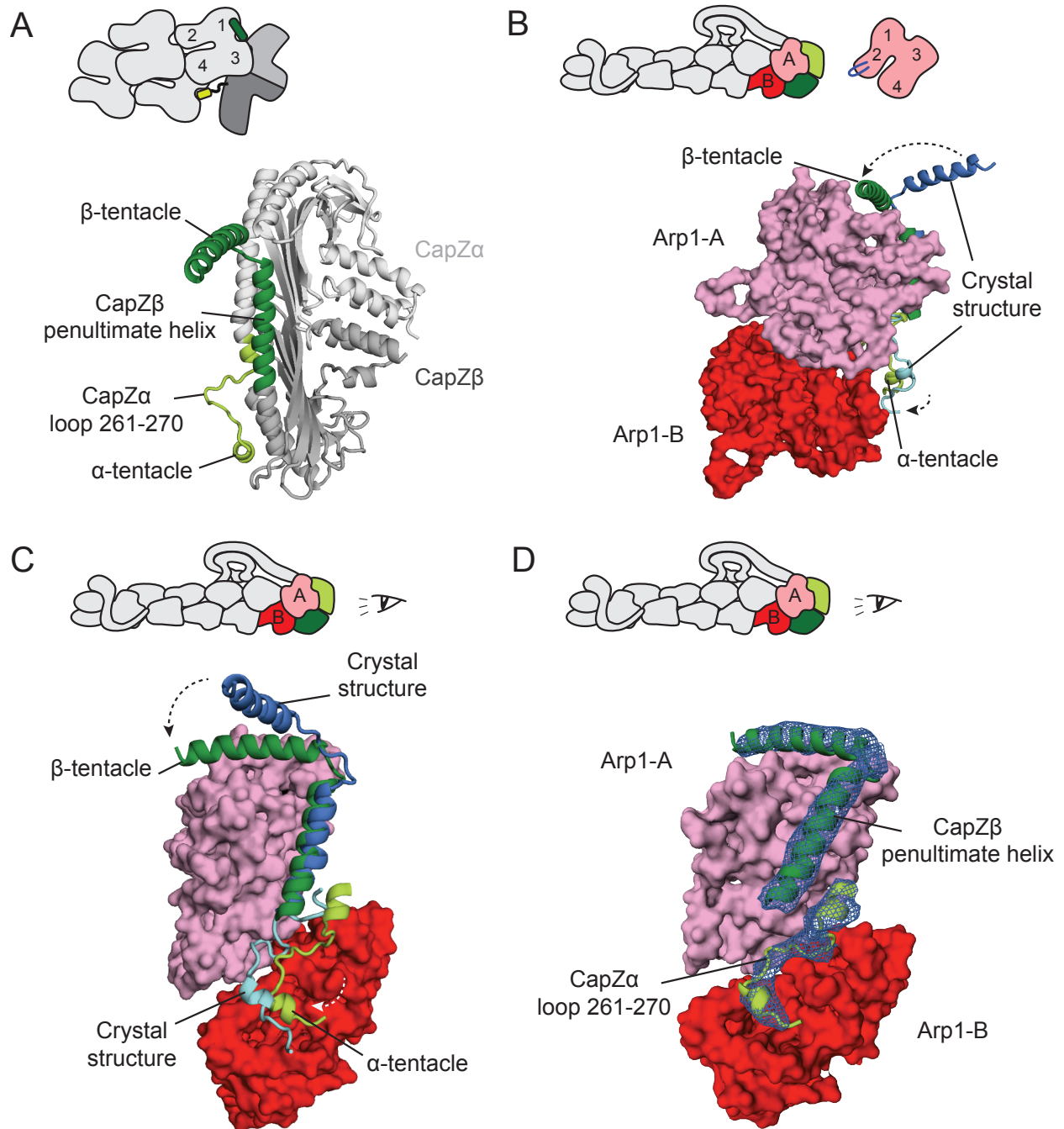
**Fig. S3.**

**The cryo-EM density in the filament is sufficient to distinguish  $\beta$ -actin from Arp1.** (A) The comparison of side chains of the cryo-EM map (sharpened and low-pass filtered to 3.5Å resolution) shows clear differences between Arp1 (pink, subunit-F) and  $\beta$ -actin (cyan, subunit-H). Four representative residue pairs have been selected (black arrows). A helix from residues D222 to S230 of  $\beta$ -actin-H (green bar in B) clearly distinguishes subunit-H as  $\beta$ -actin as the corresponding helix in Arp1 is much shorter. (B) Sequence alignment of  $\beta$ -actin and Arp1. Identical (white letter in red background), similar (red letter in white background) and dissimilar residues.



**Fig. S4.**

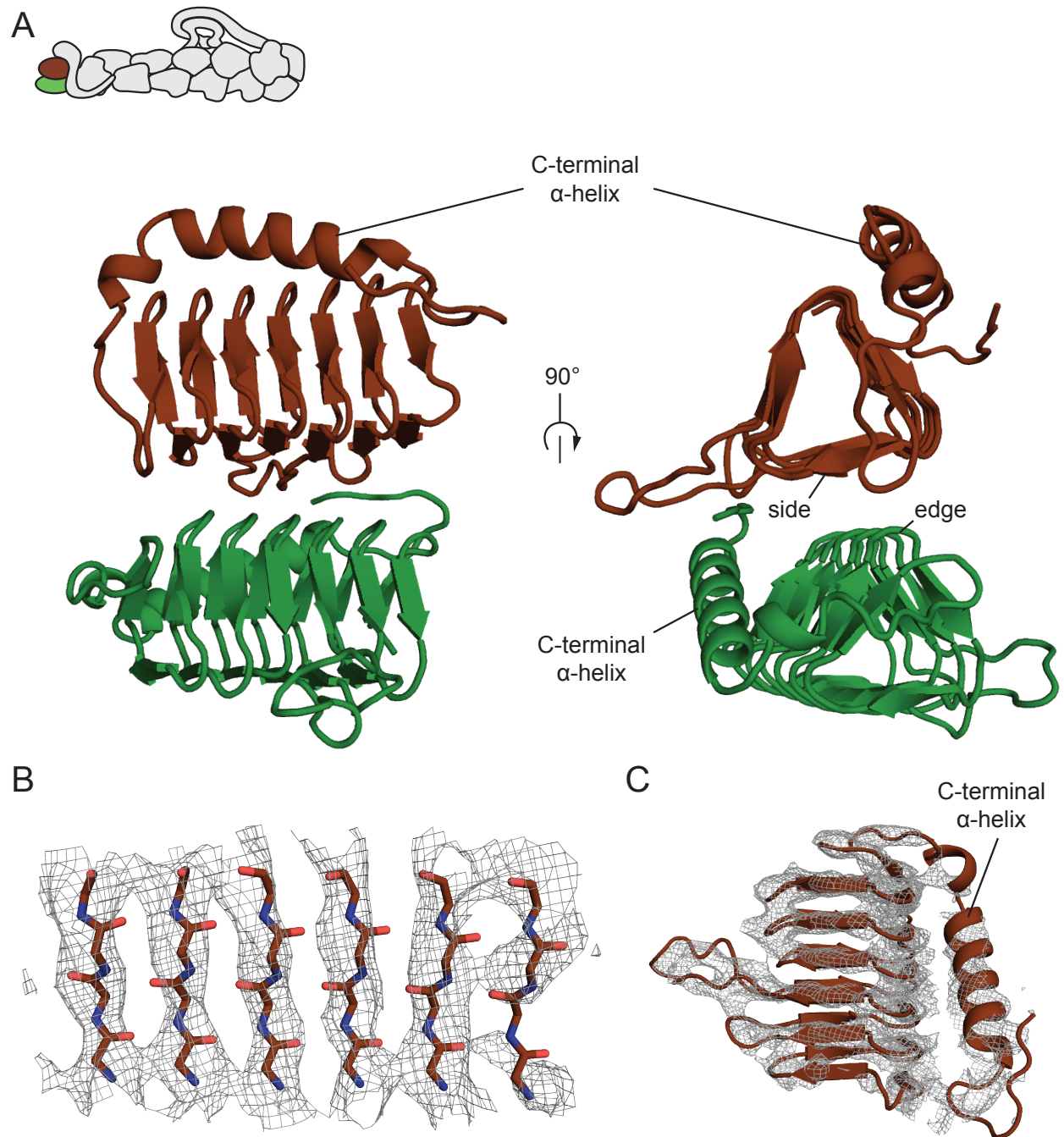
**Actin related protein 1 (Arp1) is structurally similar to  $\beta$ -actin.** Arp1 (orange) and  $\beta$ -actin (blue) monomers contain four subdomains surrounding a nucleotide binding site (ADP). The subdomain-2 loop (Arp1<sup>36-74</sup>,  $\beta$ -actin<sup>32-70</sup>) forms contacts with the hydrophobic groove between subdomains 1 and 3 of the neighboring subunit in filaments of Arp1 or  $\beta$ -actin.



**Fig. S5.**

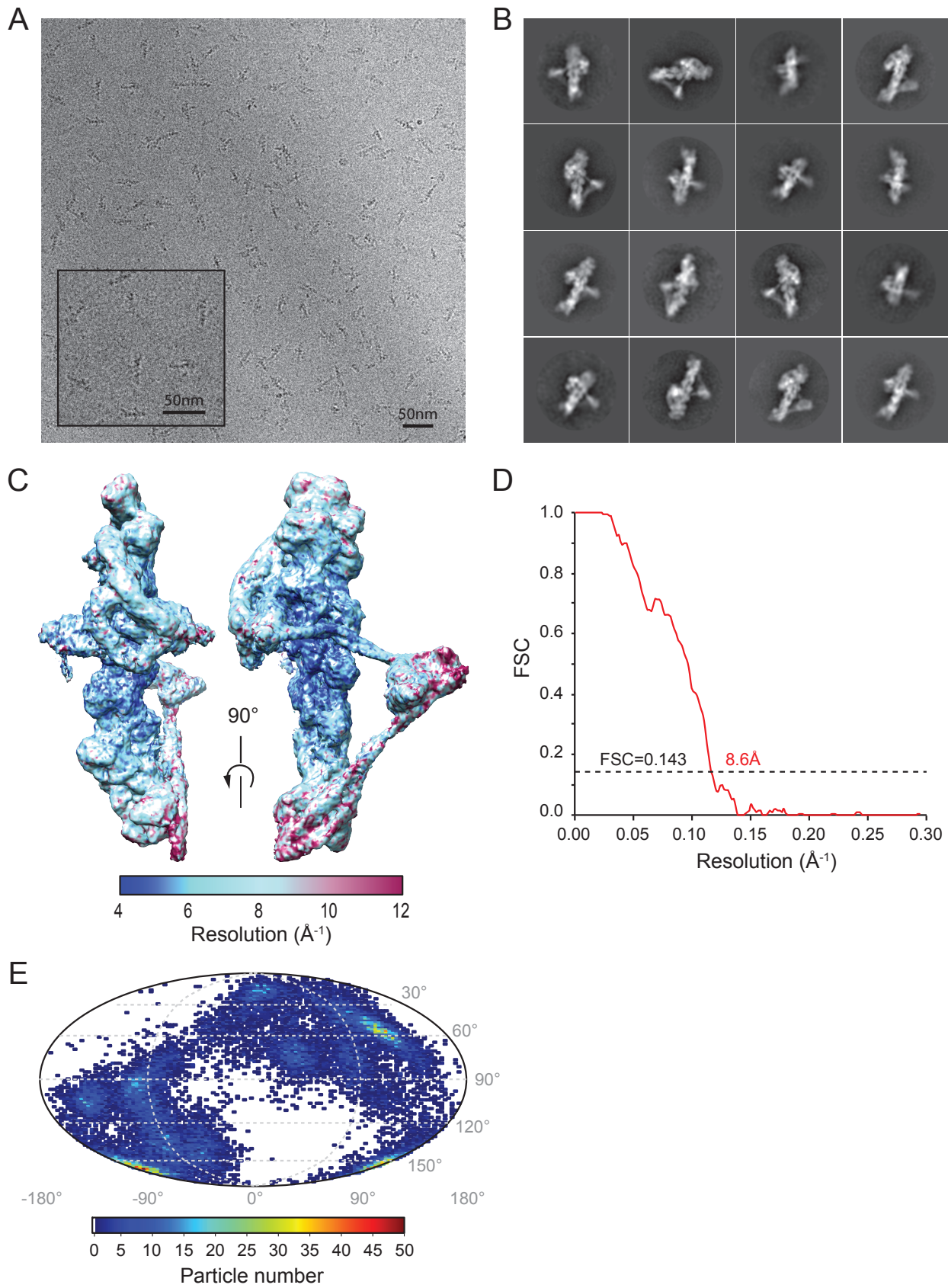
**The barbed end of the dynactin filament is capped by a CapZ $\alpha\beta$  heterodimer.** (A) Cartoon representation of CapZ $\alpha\beta$  model. (B,C) CapZ $\alpha$  and CapZ $\beta$  C-terminal helices (tentacles) rotate relative to the free CapZ $\alpha\beta$  structure (21) and fit into the hydrophobic grooves between subdomains 1&3 of Arp1-B and Arp1-A respectively. (D) 6.3Å density map and the fitted model showing that CapZ $\alpha\beta$  also contacts the end of the filament via the interaction of the penultimate helix of CapZ $\beta$  (CapZ  $\beta^{209-243}$ ) with Arp1-A and via the loop between the  $\alpha$ -tentacle (CapZ  $\alpha^{261-270}$ ) with the interface between Arp1-A and Arp1-B.





**Fig. S6.**

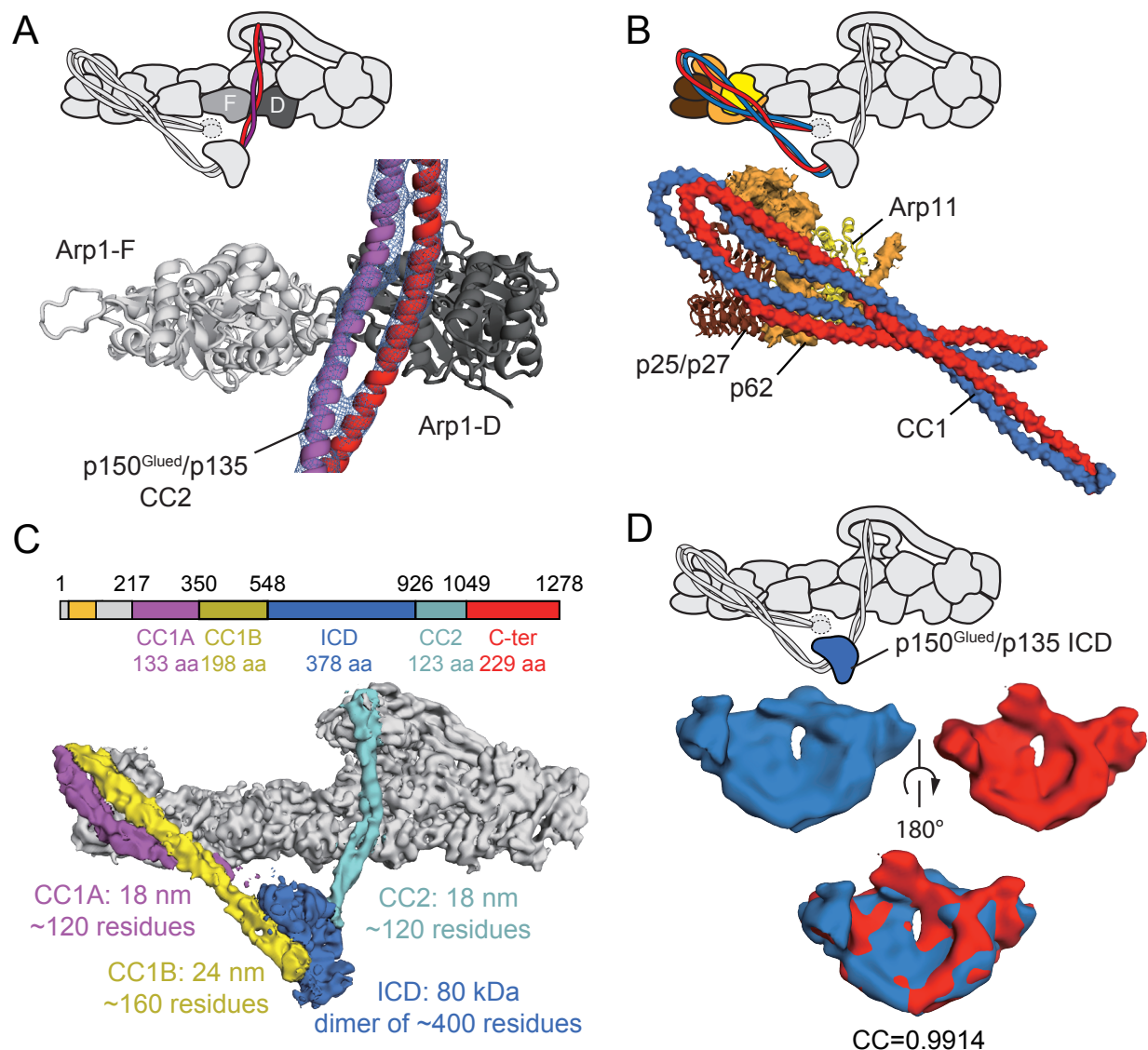
**Heterodimer of p25 and p27 in the pointed end complex.** (A) The p25 and p27 subunits each consist of a left-handed  $\beta$ -helical fold (22) followed by an  $\alpha$ -helix at the C-terminus. They pack in an edge to side configuration. (B,C) Mesh representations of the 4.0Å cryo-EM map.





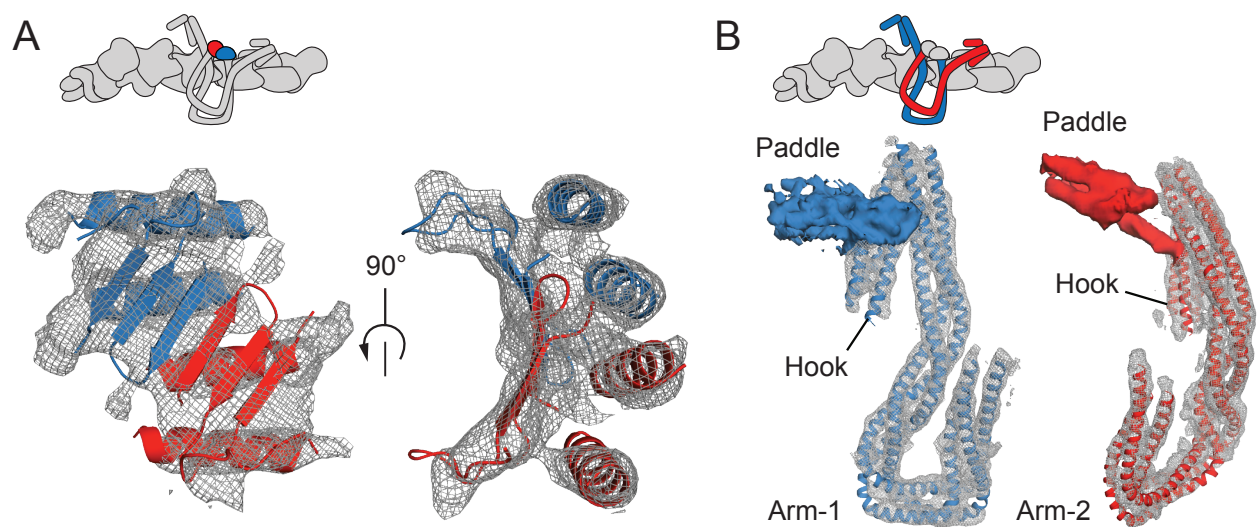
**Fig. S7.**

**Cryo-EM analysis of a subset of pig dynactin particles that have a long projection docked against their side.** (A) A representative micrograph of dynactin. (B) Typical 2D class averages obtained from a subset of particles after 3D classification that contain a long projection docked against their side. (C) The final dynactin map was analyzed by ResMap (60) showing resolution distribution from 5 to 6 Å. The resolution of the projections varies from 8 Å to 12 Å. (D) The gold-standard FSC curves of the final map. The resolution at FSC=0.143 is 8.6 Å. (E) An equal area projection map of the orientation angles of the 12,870 particles.



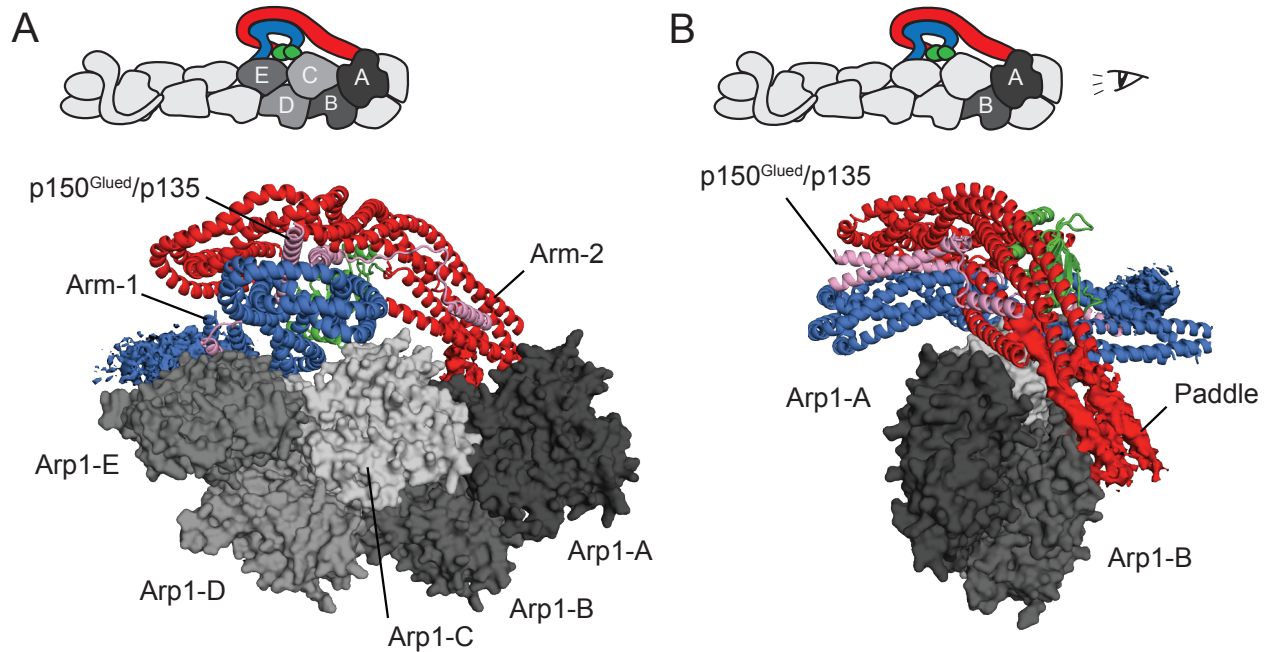
**Fig. S8.**

**The interaction of the p150<sup>Glued</sup>/p135 projection with the main body of dynactin.** (A) The p150<sup>Glued</sup>/p135 CC2 exits the shoulder and docks in a groove between Arp1 subunits D & F. (B) CC1 docks on the side of the pointed end complex. Individual helices in CC1 are shown in surface representation (red and blue). A cartoon representation is used for p25/27 (brown) and Arp11 (yellow), whereas 4.0Å cryo-EM density is used for p62 (orange). (C) The lengths of the predicted coiled coil (CC1A, CC1B, CC2) regions in the p150<sup>Glued</sup>/p135 protein match those of the coiled coil regions in the projection observed in our 8.6Å resolution map (assuming 1.5Å/residue). The size of the inter-coiled domain (ICD) also matches the number of amino acids calculated from the predicted mass of the globular domain in the cryo-EM map. (D) The globular ICD domain contains two-fold rotational symmetry, suggesting it is a dimer. Overlap of rotated maps (blue is before and red is after rotation), low pass filtered to 12Å results in a 0.99 cross-correlation coefficient.



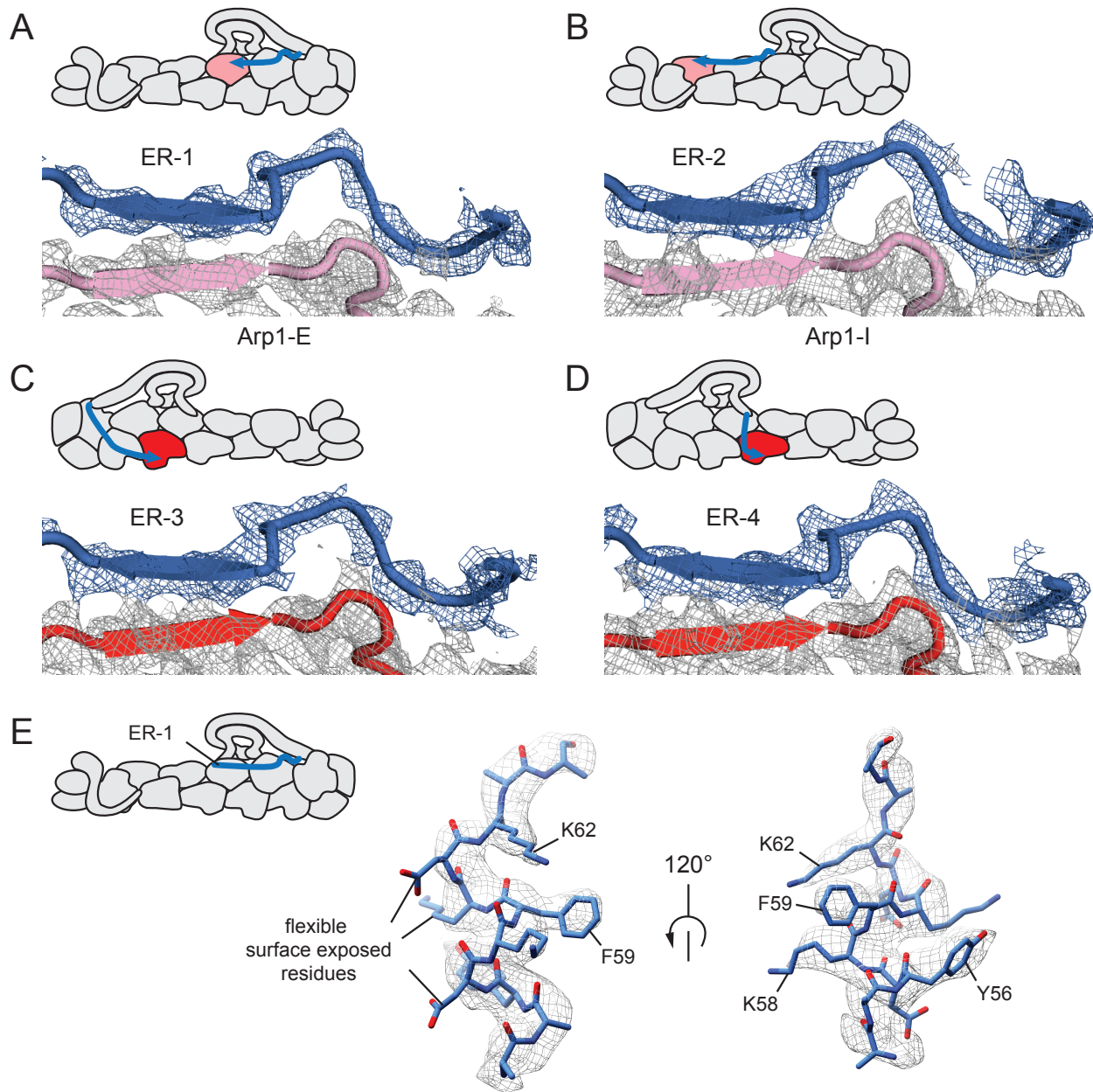
**Fig. S9.**

**6.3Å cryo-EM density in the dynactin shoulder.** (A) The dimerization domain contains two-fold internal symmetry. It is modeled as a curved  $\beta$ -sheet with 4  $\alpha$ -helices on one side. (B) A comparison of the two arms of the dynactin shoulder suggests that they are structurally similar.



**Fig. S10.**

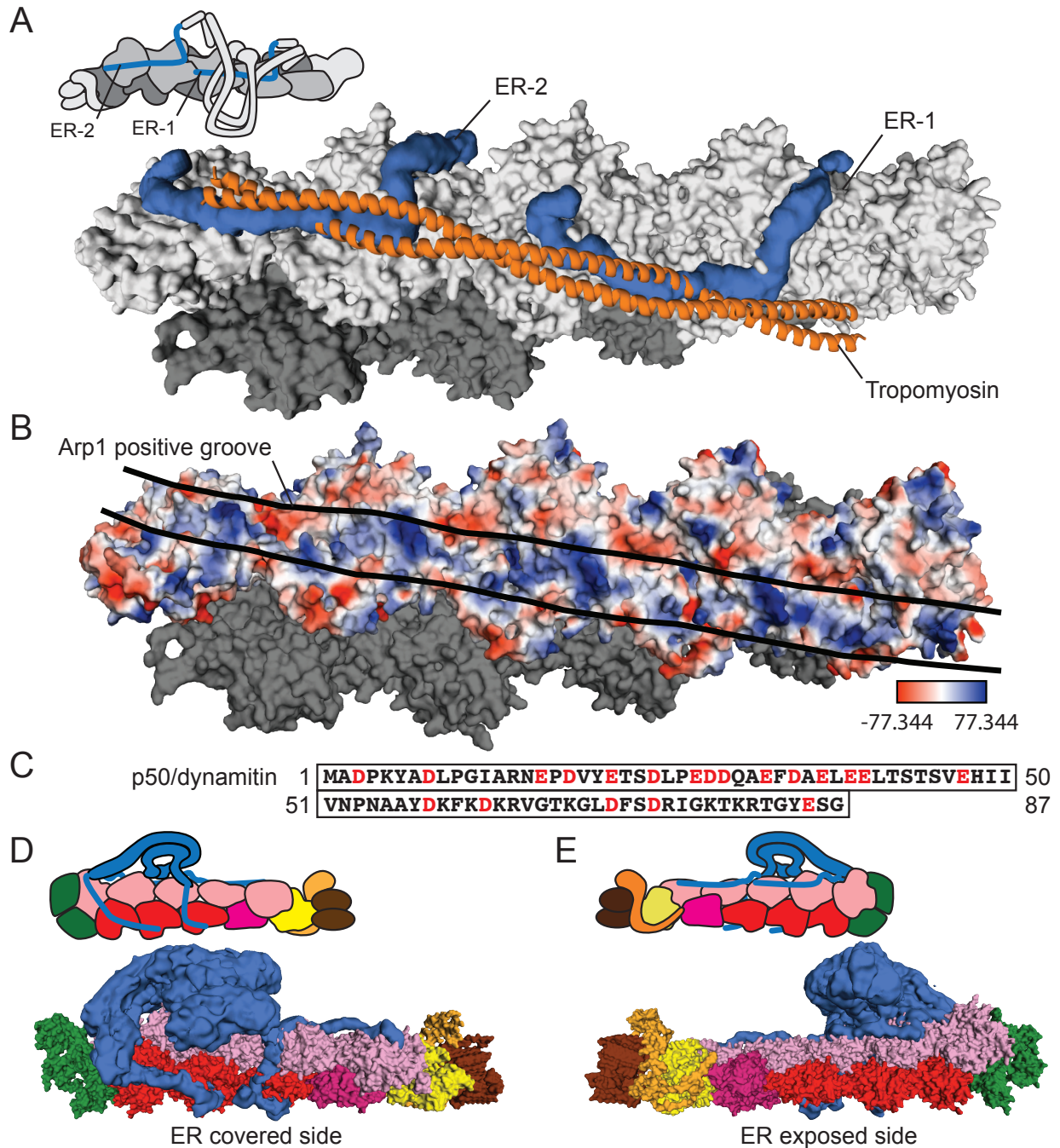
**The shoulder contacts the top protofilament.** (A) The shoulder contacts the top protofilament via subunits Arp1-A, Arp1-C and Arp1-E (B) The view from barbed end of dynactin shows that the paddle domain (surface representation of 4.0Å cryo-EM density) of arm-2 reaches down to contact subunit Arp1-B of the bottom protofilament.



**Fig. S11.**

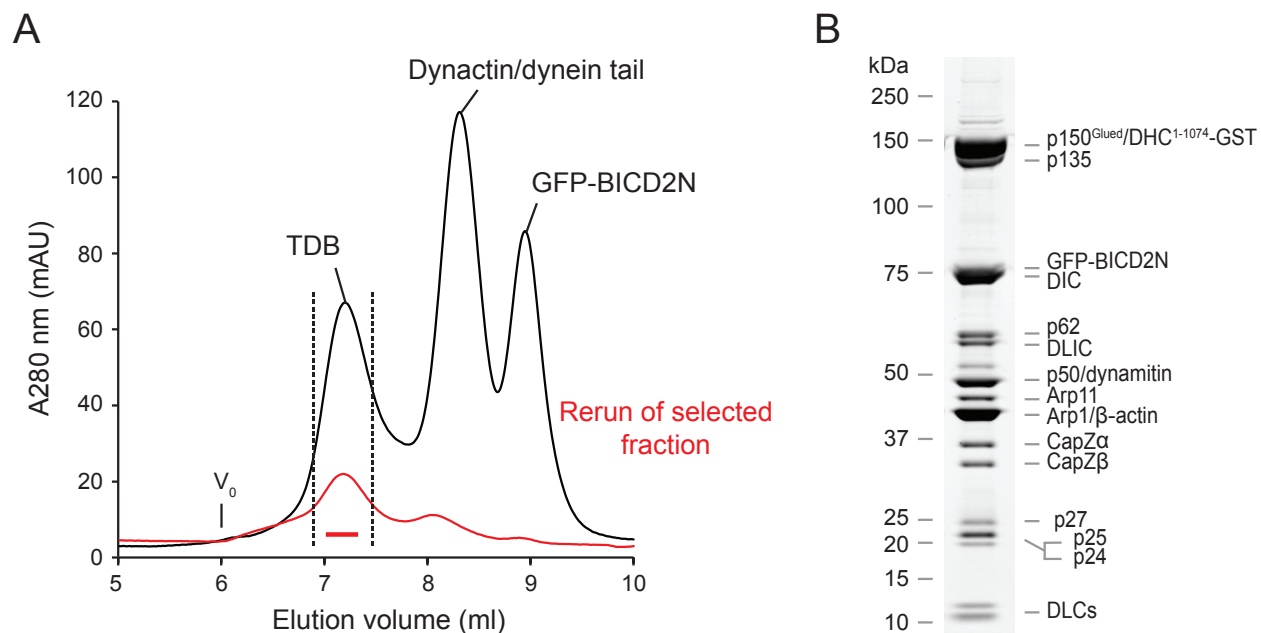
**The four extended peptides emerging from the shoulder are structurally identical and likely to be the N-termini of p50/dynamitin.** (A-D) Each of the ERs (blue) interacts with either the top (Arp1-E & I, pink) or bottom (Arp1-D & F, red) protofilament in the same way. The ERs have a distinctive curved structure toward the end, followed by a  $\beta$ -strand that hydrogen bonds to the  $\beta$ -sheet in subdomain-3 of the Arp1 subunit. A mesh representation of EM density low-pass filtered and sharpened to 3.7Å resolution is shown. (E) The side chains of buried residues from a stretch of the p50 N-terminus (Y56, K58, F59 and K62) fit into the ER-1 density (mesh representation of EM density low-pass filtered and sharpened to 3.7Å resolution).





**Fig. S12.**

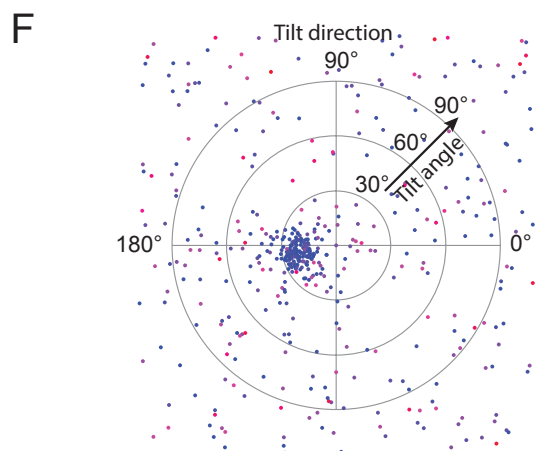
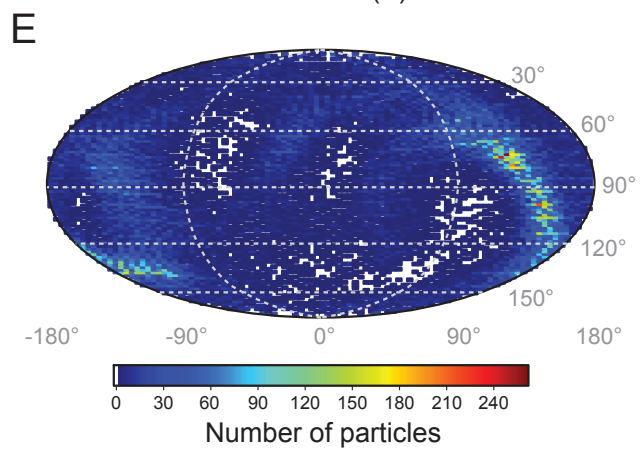
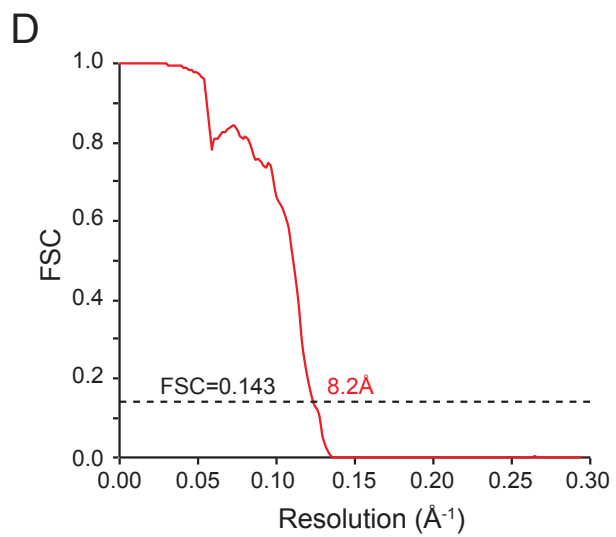
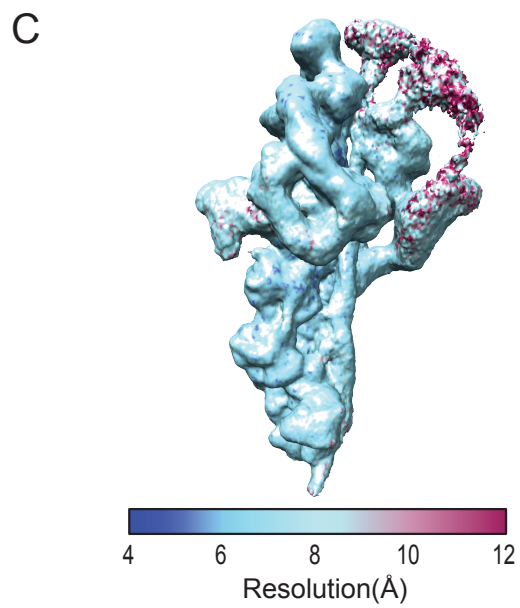
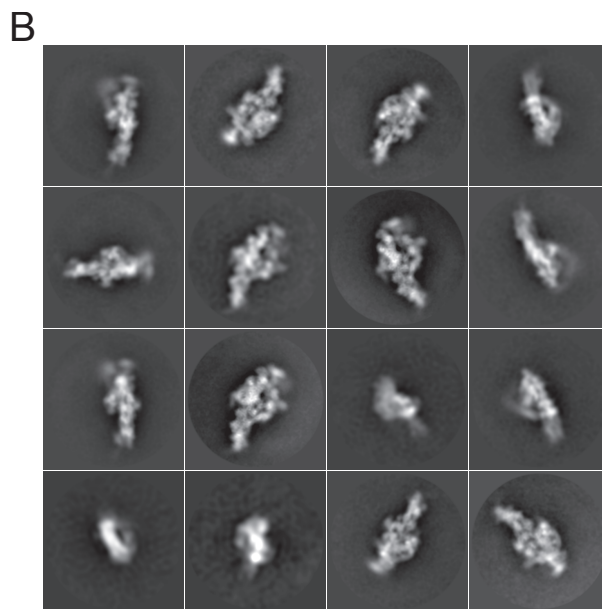
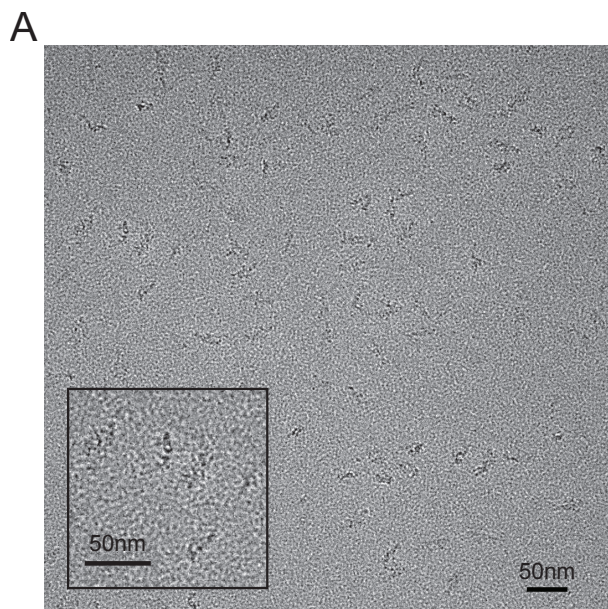
**The shoulder main body and ER peptides cover three sides of the dynactin filament. (A)** The peptides ER-1 and ER-2 (blue - 6.3Å map sharpened and low-pass filtered to 8Å resolution) bind in a groove on the Arp1 filament that is equivalent to the one that tropomyosin (orange) occupies on actin (PDB ID: 4A7H, cartoon representation). **(B)** An electrostatic surface representation of the Arp1 filament showing the positively charged groove (outlined in black) that binds the ERs. **(C)** The p50/dynamitin N-terminus sequence with negatively charged residues in red. **(D)** The shoulder main body and extended regions coat the top, bottom and back of the dynactin filament. **(E)** The front surface of the dynactin filament is left exposed.



**Fig. S13.**

**Formation of pig dynactin, human dynein tail and mouse BICD2N complex (TDB).**

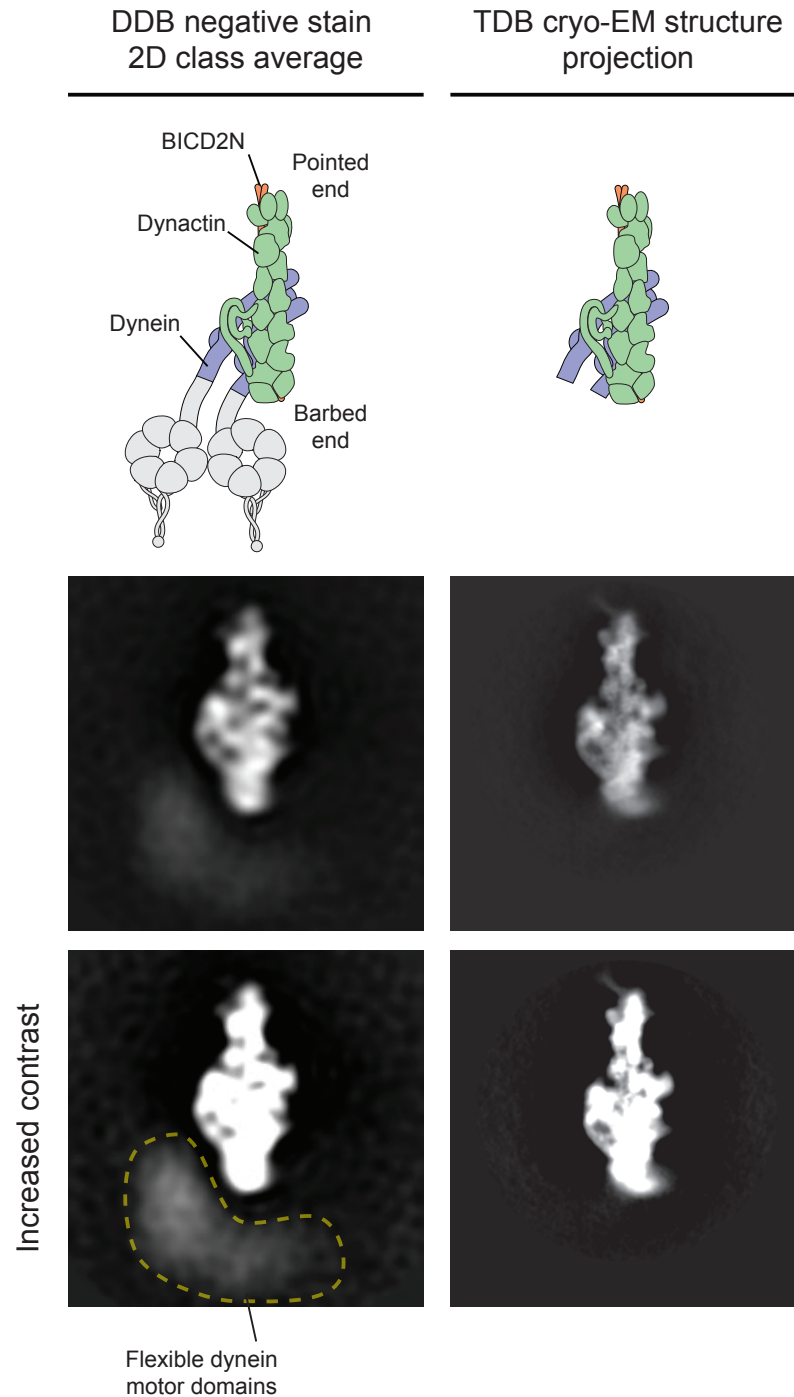
We used a human dynein tail construct containing the N-terminus of the dynein heavy chain (DHC<sup>1-1074</sup>), the intermediate chain (DIC2), light intermediate chain (DLIC1) and three light chains (Roadblock, Tctex and LC8). The TDB complex was formed by mixing this tail construct with endogenous pig dynactin and mouse BICD2N (GFP-BICD2<sup>1-400</sup>). **(A)** Black trace: size-exclusion chromatography trace for a mixture of dynactin, dynein tail and BICD2N (molar ratio of 1 dynactin complex : 2 dynein dimeric tail complexes : 14 BICD2N dimers). Red trace: rerun of the pooled and concentrated TDB complex fractions (indicated by vertical dashed lines) collected in the first run (black trace). Pooled and concentrated TDB fractions of the rerun (indicated by a red bar) were used for cryo-EM grid preparation.  $V_0$  indicates the void volume of the column. **(B)** SYPRO Ruby-stained SDS-PAGE gel of the pooled and concentrated fractions collected from the TDB peak (indicated by a red bar in A) with indicated components.





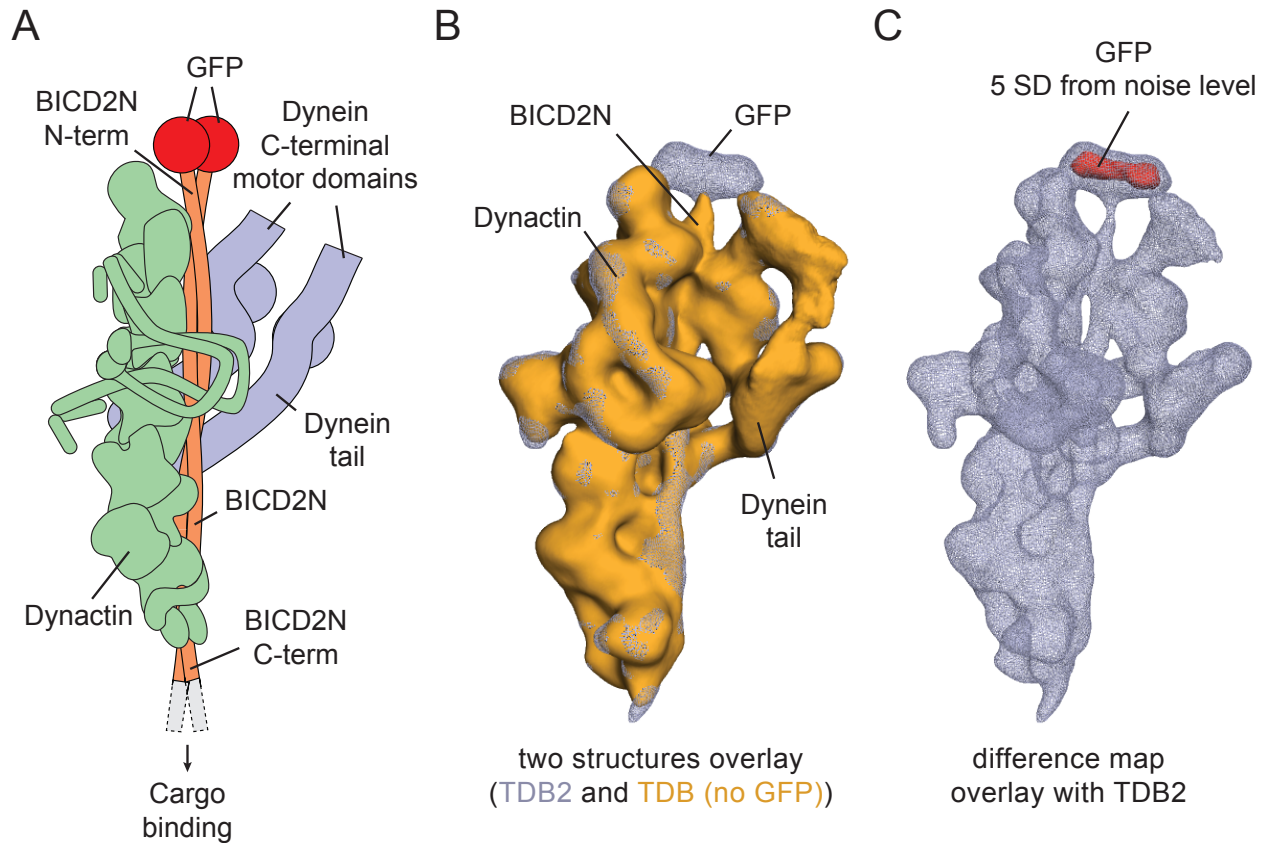
**Fig. S14.**

**Single particle cryo-EM analysis of dynein tail, dynactin and BICD2N complex (TDB).** (A) A representative micrograph of TDB complex. (B) Typical 2D class averages. (C) Final dynactin map was analyzed by ResMap showing resolution distribution from 6 to 8Å. Some of the interior parts of the map have resolution of 5-6Å. (D) The gold-standard FSC curves of the final map. The resolution at FSC=0.143 is 8.2Å. (E) An equal area projection map of the orientation angles of the 12,870 particles. (F) Tilt-pair analysis of TDB. Images were recorded at 0° and 20° tilt angle. The position of each dot represents the direction and angle for a particle pair in polar coordinates. In-plane and out-of-plane tilt transformations are shown in blue and red respectively. The blue dots cluster at a tilt angle of approximately 20°, which validates the structure.



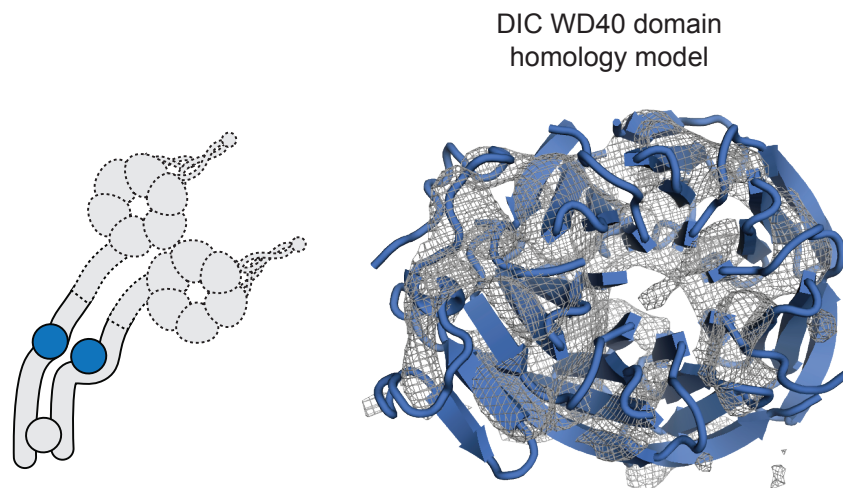
**Fig. S15.**

**The dynein tail interacts with dynactin in the same way as full length dynein.** A negative stain 2D class average of the dynein, dynactin, BICD2N (DDB) complex is highly similar to a 2D projection of the TDB complex. This suggests that the dynein tail construct interacts with dynactin in the same way as full length dynein. Flexible dynein motor domains are seen as a blur in the higher contrast image of DDB (lower panel). Comparison with the TDB projections shows that the motor domains in DDB are close to the barbed end of dynactin.



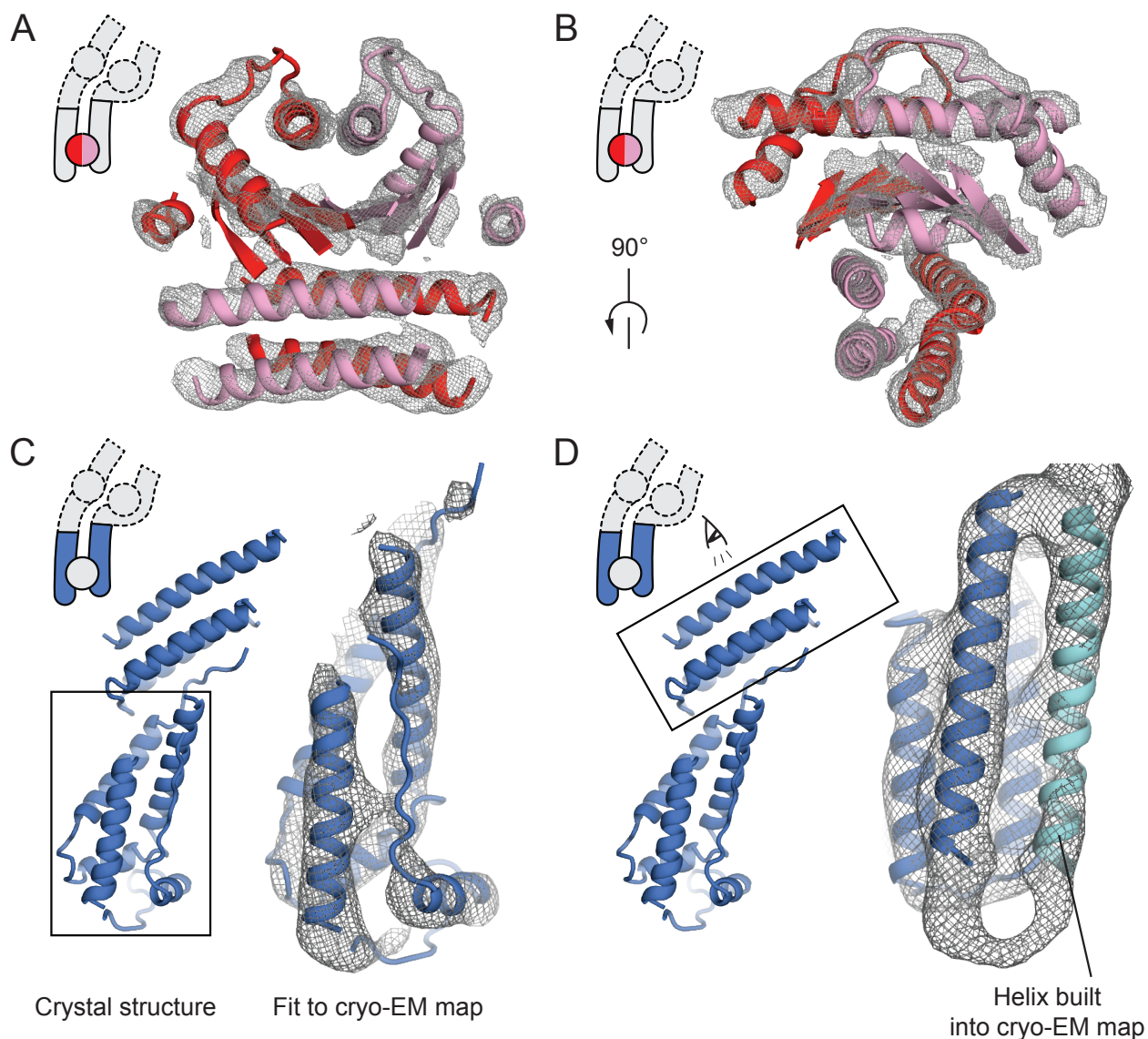
**Fig. S16.**

**N-terminus of the BICD2N is located by the barbed end.** (A) Cartoon model of dynein tail (blue), dynactin (green) and GFP-BICD2N (GFP - red, BICD2N - orange) complex (TDB). (B) A TDB complex was formed with untagged BICD2N (orange) and its low resolution structure was solved. The overlay with a TDB structure containing GFP-BICD2N (blue) shows that the two structures are nearly identical. The only difference is the absence of globular density by the barbed end in the TDB (BICD2N) structure. (C) The difference map at a threshold of 5 SD away from the noise level clearly shows that the only difference between the two complexes is the globular domain. As the globular domain also matches the expected size for two copies of GFP this suggests that the N-terminus of BICD2N is located by the barbed end.



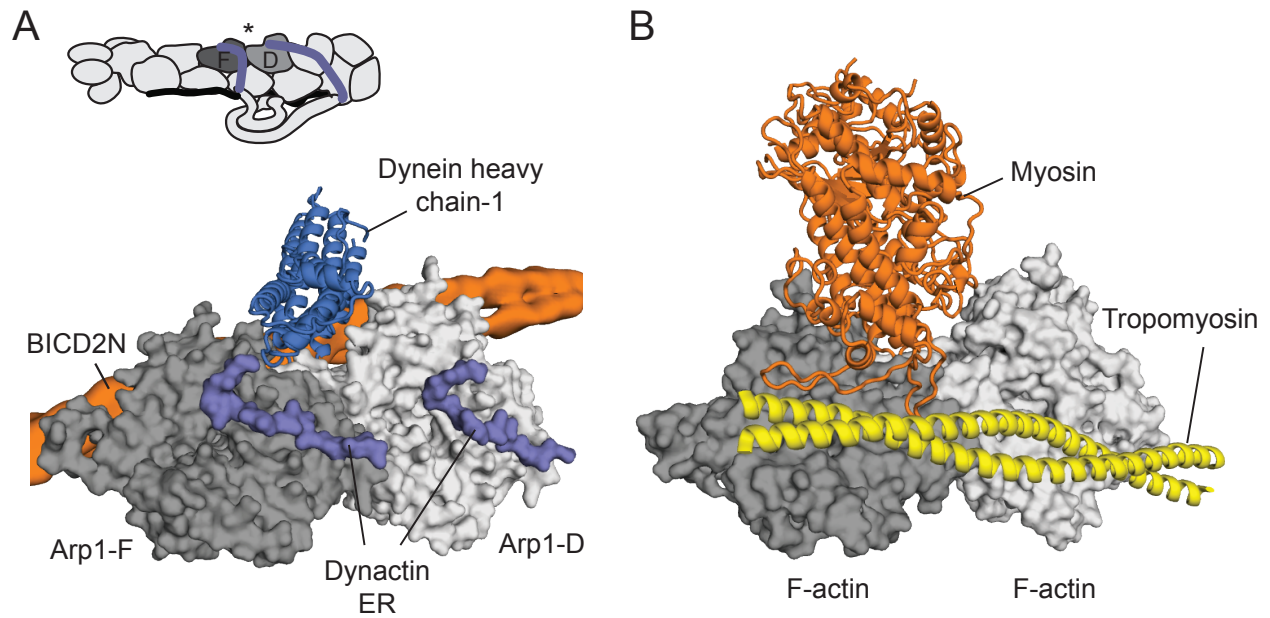
**Fig. S17.**

**The dynein intermediate chain WD40  $\beta$ -propeller domain fits the circular density in the cryo-EM map of the dynein tail.** Top view of a fit of a homology model of the dynein intermediate chain WD40  $\beta$ -propeller domain fit into cryo-EM density. The homology model was generated using Phyre2 with 1ERJ (PDB ID) as a reference.



**Fig. S18.**

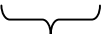

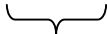
**Crystal structure of *S. cerevisiae* N-terminal 557 residues of dynein heavy chain (Dyn1<sup>1-557</sup>).** (A,B) Experimental electron density map derived from X-ray crystallography (contoured to  $2\sigma$ ) and initial model of Dyn1<sup>1-557</sup> N-terminal dimerization domain (residues 1-178). The dimerization domain consists of a central  $\beta$ -sheet flanked by  $\alpha$ -helices. Initial phases were obtained using the multiple isomorphous replacement with anomalous signal (MIRAS) approach on a selenomethionine derivative of Dyn1<sup>1-557</sup>. The map was generated after performing density modification on initial phases. The initial model was built by placing secondary structure elements into density. Assignment of residues was based on secondary structure predictions and selenomethionine positions. (C) Crystal structure of elongated domain of Dyn1<sup>1-557</sup> (residues 181-410) formed by two bundles of helices. The inset shows Dyn1<sup>1-557</sup> fitted into cryo-EM density. (D) An extra helix modeled into cryo-EM density, which was not clearly visible in the crystal density map.



**Fig. S19.**

**S19. Dynein heavy chain (DHC) binds the same cleft of the dynactin filament as myosin binds F-actin.** (A) The DHC chain-1 fits into the cleft between Arp1-D and Arp1-F. (B) The myosin motor domain occupies the equivalent site on F-actin (PDB ID: 4A7F).

**Table S1.** Cryo-EM data collection and processing summary.

	<b>Dynactin-1</b>	<b>Dynactin-2</b>	<b>Dynactin-3</b>	<b>Dynactin-4</b>	<b>TDB</b>	<b>TDB<sup>g</sup></b>	<b>TDB (no GFP)</b>
Microscope	Titan Krios	Polara	Titan Krios	Titan Krios	Titan Krios	Titan Krios	Titan Krios
Voltage (kV)	300	300	300	300	300	300	300
Detector	Falcon II	Falcon II	Falcon II	Falcon II	Falcon II	Falcon II	Falcon II
Frames	51 <sup>a</sup>	34	34	34	51	51	51
Exposure time (sec)	3	2	2	2	3	3	3
Total dose ( $\bar{\epsilon}/\text{\AA}^2$ )	51	80	54	86	51	51	51
Microscope sessions	5	3	4	4	4	4	1
Micrographs <sup>b</sup>	4,483	2,166	6,297	5,960	4,259	354	464
Pixel size ( $\text{\AA}$ )	1.7 <sup>c</sup>	1.14	1.34	1.05	1.7	1.7	1.7
Box size (original)	360	514	432	556	360	360	360
Box size (scaled)	N/A	432	432	432	N/A	N/A	N/A
Raw particles <sup>d</sup>	446,308	81,943	358,719	256,698	257,608	22,146	21,204
							
Final particles <sup>e</sup>	80,865		115,044		85,744	6,445	6,102
Final resolution <sup>f</sup>	6.3 $\text{\AA}$		4.0 $\text{\AA}$		8.2 $\text{\AA}$	11.8 $\text{\AA}$	12.5 $\text{\AA}$
Final particles (p150 <sup>Glued</sup> )	12,870						
Final resolution (p150 <sup>Glued</sup> )	8.6 $\text{\AA}$						

<sup>a</sup> – Including one data set at 34 frames.

<sup>b</sup> – Number of micrographs used for processing.

<sup>c</sup> – Including one data set at 1.34  $\text{\AA}$  and scaled to 1.7  $\text{\AA}$ .

<sup>d</sup> – Particles after autopicking and manually screening.

<sup>e</sup> – Particles used in the final reconstruction.

<sup>f</sup> – Gold standard FSC at 0.143 criterion.

<sup>g</sup> – A roughly equivalent amount of data to TDB (no GFP) was taken from the TDB dataset and processed in the same way as TDB (no GFP).



**Table S2.** Model building and refinement summary.

<b>Proteins</b>	<b>Model type</b>	<b>Building, Fitting and Refinement</b>
Arp1	Complete model with residues assigned and side chains built	Built de novo and refined automatically in Refmac5 and manually using Coot
$\beta$ -actin	Complete model with residues assigned and side chains built	Built de novo and refined automatically in Refmac5 and manually using Coot
Arp11	Complete model with residues assigned and side chains built	Built de novo and refined automatically in Refmac5 and manually using Coot
CapZ $\alpha\beta$	Backbone model with residues assigned	Model predicted by Phyre2, truncated to poly-Ala, then fit into density using Coot
p25/p27	Backbone model with residues assigned	Model predicted by Phyre2, truncated to poly-Ala, then fit into density using Coot
p62	Backbone model without residues assigned	Backbones traced through density using Coot without homology reference
Main shoulder (p24/p50/p150 <sup>Glued</sup> )	$\alpha$ -helices without subunits assigned or side chains	Helices identified and fit into density using Coot
p150 <sup>Glued</sup> (CC1, CC2)	$\alpha$ -helices with domains assigned	Helices identified and fit into density using Coot, domains assigned using predicted lengths
p150 <sup>Glued</sup> (ICD)	No model, density identified	N/A
ER-1 to ER-4 (peptides on filament)	Partial model with some residues assigned and some side chains	Built de novo and refined manually using Coot



**Table S3.** Refinement of the dynactin filament (Arp1-A to Arp1-I,  $\beta$ -actin-H and Arp11).

<b>Model composition</b>	
Non-hydrogen atoms	29,688
Protein residues	3,720
Ligands (ADP/ATP/Mg <sup>2+</sup> )	9/1/10
<b>Refinement statistics</b>	
Resolution	257.28 - 3.50
Map sharpening B-factors ( $\text{\AA}^2$ )	-108.4
Rfactor*	0.368
Overall FSC†	0.690
Correlation coefficient	0.933
Mean B-factor ( $\text{\AA}^2$ )	97.66
<b>Rms deviations</b>	
Bond length ( $\text{\AA}$ )	0.0065
Bond angle ( $^\circ$ )	1.1519
Chiral volume ( $\text{\AA}^3$ )	0.0666
<b>Validation</b>	
MolProbity score	1.83 (100 <sup>th</sup> percentile)
Clashscore, all atoms	1.28 (100 <sup>th</sup> percentile)
Good rotamers	95.18%
<b>Ramachandran plot</b>	
Favored	92.76%
Outliers	0.57%
C $\beta$ deviations >0.25 $\text{\AA}$	0.15%

\*Rfactor =  $\Sigma||F_{\text{obs}}| - |F_{\text{calc}}|| / \Sigma|F_{\text{obs}}|$ , in which  $|F_{\text{obs}}|$  is the amplitude of simulated reflections from EM map and  $|F_{\text{calc}}|$  is the amplitude of calculated reflections from the coordinates.

† Fourier Shell Correlation,  $\text{FSC}_{\text{overall}} = \Sigma(N_{\text{shell}} \text{FSC}_{\text{shell}}) / \Sigma(N_{\text{shell}})$ , where  $\text{FSC}_{\text{shell}}$  is the FSC in a given shell,  $N_{\text{shell}}$  is the number of 'structure factors' in the shell.  $\text{FSC}_{\text{shell}} = \Sigma(F_{\text{model}} F_{\text{EM}}) / (\sqrt{\Sigma(|F_{\text{model}}|^2)}) \sqrt{\Sigma(F_{\text{EM}}^2)}$ .

**Table S4.** Mass spectrometry-based proteomics of dynactin.

	<b>Protein</b>	<b>Peptide counts (all)</b>	<b>Peptide counts (unique)</b>	<b>iBA Q ratio</b>	<b>Sequence coverage (%)</b>	<b>Theoretical Mass (Da)</b>	<b>Experimental mass (Da)*</b>	<b>Mass error (%)</b>
<b>Individual subunits</b>	$\alpha$ -Arp1	22	14	7.6	61.4	42,613	42,665	0.12
	$\beta$ -Arp1	14	6	-	63.9	42,293	-	-
	p150/p135	54;51	54;51	-	45.7	141,139; 119,450	-	-
	p50	19	19	-	45.7	49,626	-	-
	p24	8	8	-	46.8	21,165	21,330	0.78
	p62	15	15	-	48.7	52,032	52,695	1.27
	p25	3	3	-	17.2	19,188	-	-
	p27	5	5	-	22.6	20,681	20,594	-0.42
	Arp11	14	14	-	41.2	46,197	46,070	-0.27
	$\beta$ -actin	13	13	1.0	50.7	41,736	-	-
	CapZ $\alpha$	9	9	-	38.5	33,016	32,951	-0.20
	CapZ $\beta$	12	12	-	35.3	30,628	30,529	-0.32

\*Experimental masses of individual protein subunits were obtained using denaturing LC-MS (LCT Premier) or CID experiments on a QToFII. iBAQ values are reported for Arp1  $\alpha$ - and  $\beta$ -actin since all peptides are unique in these sequences. These results represent three technical LC-MS replicates.

**Table S5.** Masses of the intact dynactin complex and subcomplexes formed during native mass spectrometry and tandem mass spectrometry (MS/MS) experiments.

	<b>Dynactin complexes</b>	<b>Theoretical mass (Da)</b>	<b>Experimental mass (Da)</b>	<b>Mass error (%)</b>
Native MS	8( $\alpha$ -Arp1) ( $\beta$ -actin) 2(p135) 4(p50) 2(p24) (p62) (p25) (p27) (Arp11) (CapZ $\alpha$ ) (CapZ $\beta$ )	1,064,116	1,066,889	0.26
MS/MS	-p27	1,043,435	1,045,724	0.22
	-CapZ $\alpha$	1,031,100	1,033,400	0.22
	-CapZ $\alpha$ , -p25	1,011,912	1,013,388	0.15
	-CapZ $\alpha$ , -CapZ $\beta$	1,000,472	1,003,204	0.27
	-CapZ $\alpha$ , -p62	979,068	981,840	0.28

**Table S6.** *S. cerevisiae* N-terminal 557 residues of dynein heavy chain (Dyn1<sup>1-557</sup>) data collection and phasing statistics.

Diffraction data	Nat <sup>a</sup>	SeMet <sub>peak</sub>	SeMet <sub>infl</sub>	SeMet <sub>Hrem</sub>
Space group	<i>P2<sub>1</sub>2<sub>1</sub>2<sub>1</sub></i>	<i>P2<sub>1</sub>2<sub>1</sub>2<sub>1</sub></i>	<i>P2<sub>1</sub>2<sub>1</sub>2<sub>1</sub></i>	<i>P2<sub>1</sub>2<sub>1</sub>2<sub>1</sub></i>
Unit cell (Å)	<i>a</i> = 71.9 <i>b</i> = 148.9 <i>c</i> = 179.6	<i>a</i> = 72.0 <i>b</i> = 149.0 <i>c</i> = 179.4	<i>a</i> = 72.1 <i>b</i> = 148.9 <i>c</i> = 179.5	<i>a</i> = 72.1 <i>b</i> = 149.2 <i>c</i> = 178.8
Unit cell (°)	$\alpha$ = 90.0 $\beta$ = 90.0 $\gamma$ = 90.0	$\alpha$ = 90.0 $\beta$ = 90.0 $\gamma$ = 90.0	$\alpha$ = 90.0 $\beta$ = 90.0 $\gamma$ = 90.0	$\alpha$ = 90.0 $\beta$ = 90.0 $\gamma$ = 90.0
Resolution (Å)	52.6 - 5.0	64.9 - 5.0	61.0 - 5.0	64.9 - 5.0
R <sub>sym</sub> <sup>b</sup>	7.7 (28.7)*	9.9 (58.2)	7.5 (41.5)	7.5 (37.1)
<I>/< $\sigma$ I>	15.8 (9.7)	12.9 (4.3)	14.7 (4.9)	14.5 (5.5)
Completeness (%)	99.9 (100.0)	99.8 (99.3)	99.8 (99.3)	99.8 (99.3)
Redundancy	11.4	9.9	9.8	9.6
n-Reflections	101,399	87,406	87,249	84,886
Wavelength (Å)	0.9763	0.9795	0.9797	0.9393
CC <sub>anom</sub> =0.3 cutoff (Å)	-	6.8	-	-
<b>Phasing statistics</b>				
FOM <sup>c</sup>	0.36	-	-	-
<b>Ramachandran plot</b>				
Favored regions (%)	98.54	-	-	-
Allowed regions (%)	1.46	-	-	-
Disallowed regions (%)	0.0	-	-	-

\*The values in parentheses refer to the highest resolution shell. <sup>a</sup>Nat is the result of merging two datasets collected from two different SeMet crystals. <sup>b</sup>R<sub>sym</sub> (I) =  $\sum hkl \sum i |I_i(hkl) - \langle I(hkl) \rangle| / \sum hkl \sum I_i(hkl)$  for n independent reflections and i observations of a given reflection. <sup>c</sup>FOM = mean figure of merit.

### Movie S1.

**Dynactin cryo-EM structure overview.** Gray surface representation of dynactin cryo-EM map at 4.0Å resolution. Segmented and colored density map represents different dynactin subunits. The 9 subunit filament contains five Arp1 subunits (pink) in the top protofilament and three Arp1 (red) and one  $\beta$ -actin-H (magenta) in the bottom protofilament. It is capped at the pointed end by a complex of Arp11 (yellow), p25 & p27 (brown) and p62 (orange) and at the barbed end by a heterodimer of capping proteins CapZ $\alpha\beta$  (green). The shoulder (blue) sits on top of the filament and contains p150<sup>Glued</sup>, p50 and p24. A cartoon representation of molecular model of dynactin colored as in segmented density.

### Movie S2.

**Cryo-EM density map and the fitted Arp1-F atomic model.** Mesh representation of Arp1-F (magenta) cryo-EM density (sharpened to 3.5Å resolution) shows the high resolution map that was used to build and refine the dynactin filament (Arp1 A&I,  $\beta$ -actin-H) and Arp11.

### Movie S3.

**The barbed end of the dynactin filament is capped by CapZ $\alpha\beta$  heterodimer.** Arp1-A and B (pink and red respectively) represented as a cartoon and transparent surface. Cartoon representation of CapZ $\alpha\beta$  model. CapZ $\alpha$  and CapZ $\beta$  (light and dark green respectively) C-terminal helices (tentacles) rotate relative to the free CapZ $\alpha\beta$  structure (21) and fit into the hydrophobic grooves between subdomains 1&3 of Arp1-B and Arp1-A respectively.

### Movie S4.

**Cryo-EM TDB structure overview.** Segmented and low-pass filtered to 12Å resolution TDB cryo-EM map. The dynein tail (blue) runs along the front face of dynactin (green) covering two thirds of the filament from  $\beta$ -actin-H to the barbed end. A long coiled coil, corresponding to BICD2N, runs the length of the filament and is sandwiched between dynactin and the dynein tail.

### Movie S5.

**5Å resolution crystal structure of the N-terminal 557 residues of the *S. cerevisiae* DHC (Dyn1<sup>1-557</sup>).** Two elongated  $\alpha$ -helical regions are joined by an  $\alpha/\beta$  domain. The Dyn1<sup>1-557</sup> structure fits well into the cryo-EM map (low pass filtered to 8Å resolution): the elongated parts of chains-1 and 2 need to be rotated by approximately 90° and 180° respectively so they run parallel to each other.

### Movie S6.

**DHC binding sites are equivalent to the myosin binding site on actin.** DHC (blue) binds in the cleft between two adjacent Arp1 subunits (gray) identical to that of the myosin (orange) binding on actin (PDB ID: 4A7H).

**Movie S7.**

**All dynein tail interactions with dynactin are mediated by BICD2N.** Surface representation of segmented TDB map low-pass filtered to either 8 or 12Å resolution. The translational symmetry observed between DHC (blue) chain-1 and 2 matches that of their binding sites on dynactin bottom protofilament (green). BICD2N (orange) stabilizes the interaction of the DHC chains with dynactin. The second interaction site of chain-1 with dynactin is solely mediated by BICD2N.

## References

1. S. R. Gill *et al.*, *J. Cell Biol.* **115**, 1639–1650 (1991).
2. M. McGrail *et al.*, *J. Cell Biol.* **131**, 411–425 (1995).
3. M. Plamann, P. F. Minke, J. H. Tinsley, K. S. Bruno, *J. Cell Biol.* **127**, 139–149 (1994).
4. V. J. Allan, *Biochem. Soc. Trans.* **39**, 1169–1178 (2011).
5. G. Schiavo, L. Greensmith, M. Hafezparast, E. M. C. Fisher, *Trends Neurosci* **36**, 641–651 (2013).
6. M. P. Dodding, M. Way, *EMBO J.* **30**, 3527–3539 (2011).
7. D. A. Schafer, S. R. Gill, J. A. Cooper, J. E. Heuser, T. A. Schroer, *J. Cell Biol.* **126**, 403–412 (1994).
8. T. A. Schroer, *Annu Rev Cell Dev Biol* **20**, 759–779 (2004).
9. A. E. Siglin *et al.*, *PLoS ONE* **8**, e59453 (2013).
10. C. Duellberg *et al.*, *Nat. Cell Biol.* **16**, 804–811 (2014).
11. S. J. King, C. L. Brown, K. C. Maier, N. J. Quintyne, T. A. Schroer, *Molecular Biology of the Cell* **14**, 5089–5097 (2003).
12. D. Splinter *et al.*, *Molecular Biology of the Cell* **23**, 4226–4241 (2012).
13. M. A. Schlager, H. T. Hoang, L. Urnavicius, S. L. Bullock, A. P. Carter, *EMBO J.* **33**, 1855–1868 (2014).
14. R. J. McKenney, W. Huynh, M. E. Tanenbaum, G. Bhabha, R. D. Vale, *Science* **345**, 337–341 (2014).
15. M. Dienstbier, X. Li, *Biochem. Soc. Trans.* **37**, 1066–1071 (2009).
16. J. L. Hodgkinson, C. Peters, S. A. Kuznetsov, W. Steffen, *Proc Natl Acad Sci U S A* **102**, 3667–3672 (2005).
17. H. Imai, A. Narita, Y. Maéda, T. A. Schroer, *J Mol Biol* **426**, 3262–3271 (2014).
18. J. B. Bingham, T. A. Schroer, *Curr. Biol.* **9**, 223–226 (1999).
19. X.-C. Bai, G. McMullan, S. H. W. Scheres, *Trends Biochem. Sci.* **40**, 49–57 (2015).
20. Materials and methods are available as supplementary materials on Science Online.

21. A. Yamashita, K. Maeda, Y. Maéda, *EMBO J.* **22**, 1529–1538 (2003).
22. T. Y. Yeh *et al.*, *EMBO J.* **32**, 1023–1035 (2013).
23. E. A. Holleran, M. K. Tokito, S. Karki, E. L. Holzbaaur, *J. Cell Biol.* **135**, 1815–1829 (1996).
24. J. von der Ecken *et al.*, *Nature* (2014), doi:10.1038/nature14033.
25. A. Narita, S. Takeda, A. Yamashita, Y. Maéda, *EMBO J.* **25**, 5626–5633 (2006).
26. F. K. Y. Cheong, L. Feng, A. Sarkeshik, J. R. Yates, T. A. Schroer, *Molecular Biology of the Cell* **25**, 2171–2180 (2014).
27. D. M. Eckley *et al.*, *J. Cell Biol.* **147**, 307–320 (1999).
28. T. Y. Yeh, N. J. Quintyne, B. R. Scipioni, D. M. Eckley, T. A. Schroer, *Molecular Biology of the Cell* **23**, 3827–3837 (2012).
29. B. Hammesfahr, M. Kollmar, *BMC Evol. Biol.* **12**, 95 (2012).
30. S. K. Tripathy *et al.*, *Nat. Cell Biol.* **16**, 1192–1201 (2014).
31. K. K. Pfister, S. E. Benashski, J. F. Dillman, R. S. Patel-King, S. M. King, *Cell Motil. Cytoskeleton* **41**, 154–167 (1998).
32. J. P. Lees-Miller, D. M. Helfman, T. A. Schroer, *Nature* **359**, 244–246 (1992).
33. E. Behrmann *et al.*, *Cell* **150**, 327–338 (2012).
34. Y. Liu *et al.*, *Genes Dev.* **27**, 1233–1246 (2013).
35. S. H. Tynan, M. A. Gee, R. B. Vallee, *J. Biol. Chem.* **275**, 32769–32774 (2000).
36. J. C. Williams *et al.*, *Proc Natl Acad Sci U S A* **104**, 10028–10033 (2007).
37. G. Benison, P. A. Karplus, E. Barbar, *J Mol Biol* **371**, 457–468 (2007).
38. M. van Spronsen *et al.*, *Neuron* **77**, 485–502 (2013).
39. I. Jordens *et al.*, *Curr. Biol.* **11**, 1680–1685 (2001).
40. T. Torisawa *et al.*, *Nat. Cell Biol.* **16**, 1118–1124 (2014).
41. J. B. Bingham, S. J. King, T. A. Schroer, in *sciencedirect.com*, *Methods in Enzymology*. (Elsevier, 1998), vol. 298, pp. 171–184.
42. T. A. Schroer, M. P. Sheetz, *J. Cell Biol.* **115**, 1309–1318 (1991).
43. R. B. Dodd *et al.*, *J. Biol. Chem.* **279**, 53840–53847 (2004).



44. T. G. G. Battye, L. Kontogiannis, O. Johnson, H. R. Powell, A. G. W. Leslie, *Acta Crystallogr. D Biol. Crystallogr.* **67**, 271–281 (2011).
45. P. Evans, *Acta Crystallogr. D Biol. Crystallogr.* **62**, 72–82 (2005).
46. C. Vonnrhein, E. Blanc, P. Roversi, G. Bricogne, *Methods Mol. Biol.* **364**, 215–230 (2007).
47. P. Emsley, K. Cowtan, *Acta Crystallogr. D Biol. Crystallogr.* **60**, 2126–2132 (2004).
48. M. D. Winn *et al.*, *Acta Crystallogr. D Biol. Crystallogr.* **67**, 235–242 (2011).
49. M. Radermacher, *J Electron Microsc Tech* **9**, 359–394 (1988).
50. X. Li *et al.*, *Nat Methods* **10**, 584–590 (2013).
51. S. H. W. Scheres, *J. Struct. Biol.* **180**, 519–530 (2012).
52. J. A. Mindell, N. Grigorieff, *J. Struct. Biol.* **142**, 334–347 (2003).
53. S. H. Scheres, *Elife* **3**, e03665 (2014).
54. P. B. Rosenthal, R. Henderson, *J Mol Biol* **333**, 721–745 (2003).
55. G. Tang *et al.*, *J. Struct. Biol.* **157**, 38–46 (2007).
56. S. H. W. Scheres, R. Núñez-Ramírez, C. O. S. Sorzano, J. M. Carazo, R. Marabini, *Nat Protoc* **3**, 977–990 (2008).
57. L. A. Kelley, M. J. E. Sternberg, *Nat Protoc* **4**, 363–371 (2009).
58. G. N. Murshudov *et al.*, *Acta Crystallogr. D Biol. Crystallogr.* **67**, 355–367 (2011).
59. E. F. Pettersen *et al.*, *J. Comput. Chem.* **25**, 1605–1612 (2004).
60. A. Kucukelbir, F. J. Sigworth, H. D. Tagare, *Nat Methods* **11**, 63–65 (2014).
61. F. Sobott, H. Hernández, M. G. McCammon, M. A. Tito, C. V. Robinson, *Anal. Chem.* **74**, 1402–1407 (2002).
62. H. Hernández, C. V. Robinson, *Nat Protoc* **2**, 715–726 (2007).
63. J. V. Olsen *et al.*, *Mol. Cell Proteomics* **4**, 2010–2021 (2005).
64. J. Cox, M. Mann, *Nat. Biotechnol.* **26**, 1367–1372 (2008).
65. B. B. Schwanhäusser *et al.*, *Nature* **473**, 337–342 (2011).